

NASA TECHNICAL NOTE



NASA TN D-6066

NASA TN D-6066

CASE FILE  
COPY

# INVESTIGATION OF A DIGITAL AUTOMATIC AIRCRAFT LANDING SYSTEM IN TURBULENCE

*by Frank Neuman and John D. Foster*

*Ames Research Center*

*Moffett Field, Calif. 94035*

NATIONAL AERONAUTICS AND SPACE ADMINISTRATION • WASHINGTON, D. C. • OCTOBER 1970



1. Report No. NASA TN D-6066		2. Government Accession No.		3. Recipient's Catalog No.	
4. Title and Subtitle <b>INVESTIGATION OF A DIGITAL AUTOMATIC AIRCRAFT LANDING SYSTEM IN TURBULENCE</b>				5. Report Date October 1970	
				6. Performing Organization Code	
7. Author(s) Frank Neuman and John D. Foster				8. Performing Organization Report No. A-3504	
				10. Work Unit No. 125-06-05-03-00-21	
9. Performing Organization Name and Address NASA Ames Research Center Moffett Field, Calif. 94035				11. Contract or Grant No.	
				13. Type of Report and Period Covered Technical Note	
12. Sponsoring Agency Name and Address National Aeronautics and Space Administration Washington, D. C. 20546				14. Sponsoring Agency Code	
15. Supplementary Notes					
16. Abstract  <p>A digital system has been studied for automatically controlling the longitudinal motion of a large transport aircraft during the landing phase. The study was carried out by means of an all-digital simulation that was chiefly concerned with investigating the effects of gusts and wind shears on aircraft control near the ground. The performance of the automatic control system operating in turbulence was determined by a Monte Carlo technique.</p> <p>With respect to the digital control system, it was found that (1) the basic analog flare mode could be modified to improve its performance under conditions of turbulence and wind shear; (2) for most control modes the computation rate requirement is surprisingly low, as indicated by the effects of computer repetition rate on the aircraft performance; (3) the performance degradation that results when a control computation cycle is occasionally skipped is relatively minor, a fact that is significant when the computer is shared with other systems for which emergency computations may have to be performed.</p> <p>Some of the causes of hard touchdowns showed the feasibility of developing a more efficient Monte Carlo technique that would aid future investigations.</p>					
17. Key Words (Suggested by Author(s))  Aircraft automatic landing Digital turbulence simulation			18. Distribution Statement  Unclassified—Unlimited		
19. Security Classif. (of this report) Unclassified		20. Security Classif. (of this page) Unclassified		21. No. of Pages 60	22. Price* \$3.00

\*For sale by the Clearinghouse for Federal Scientific and Technical Information  
Springfield, Virginia 22151



# TABLE OF CONTENTS

	<u>Page</u>
LIST OF SYMBOLS . . . . .	v
SUMMARY . . . . .	1
INTRODUCTION . . . . .	1
SIMULATION OF THE AUTOMATIC LANDING SYSTEM . . . . .	3
Mode Controller . . . . .	3
Detailed Description of the Control Modes . . . . .	5
Altitude hold mode . . . . .	5
Capture mode . . . . .	5
Glide-slope tracking mode . . . . .	6
Flare mode . . . . .	7
REPRESENTATION OF ATMOSPHERIC TURBULENCE FOR AIRPLANE SIMULATION . . . . .	10
Background . . . . .	10
Simulation . . . . .	13
Digital simulation equations . . . . .	14
Properties of the turbulence model . . . . .	16
TECHNIQUES FOR ANALYZING THE SIMULATED FLIGHTS . . . . .	17
Statistical Analysis . . . . .	17
Paired Observations . . . . .	19
AUTOMATIC CONTROL SYSTEM PERFORMANCE . . . . .	19
Comparison of Analog and Digital Control System Performance . . . . .	19
Performance of the Noncritical Control Modes . . . . .	20
Performance of the Critical Control Modes Under Steady Wind Conditions and Simple Shear . . . . .	21
Performance of the Critical Control Modes Under Turbulent Conditions . . . . .	23
Glide-slope tracking . . . . .	23
Flare mode . . . . .	24
Touchdown Performance of the Landing System . . . . .	29
Performance of the System With Reduced Sampling Rates . . . . .	30
Performance of the System With Randomly Missing Computation Cycles . . . . .	32
CONCLUSIONS . . . . .	33
APPENDIX A – SIMULATION OF THE STABILIZED AIRPLANE . . . . .	34
AIRPLANE EQUATIONS . . . . .	34
Equations of Motion . . . . .	34
Engine and Engine Servos . . . . .	39
Elevator, Elevator Servo, and Flaps . . . . .	39

## TABLE OF CONTENTS

	<u>Page</u>
AUTOMATIC FLIGHT-PATH STABILIZATION . . . . .	40
Pitch Control Loop . . . . .	40
Autothrottle . . . . .	40
APPENDIX B – SIMULATION OF LINEAR SYSTEMS WITH DIFFERENCE EQUATIONS. . . . .	42
APPENDIX C – FILTER GAIN CONSTANT ADJUSTMENT FOR THE DIGITAL TURBULENCE SIMULATION. . . . .	48
REFERENCES . . . . .	51

## LIST OF SYMBOLS

$C_D$	drag coefficient, $D/(1/2)\rho V^2 S$
$C_L$	lift coefficient, $L/(1/2)\rho V^2 S$
$C_m$	pitching-moment coefficient, pitching moment/ $(1/2)\rho V^2 S \bar{c}$
$C_{m_0}$	$C_m$ at zero angle of attack
$\bar{c}$	wing mean aerodynamic chord, ft
cg	center of gravity
$D$	aerodynamic drag, lb
$d$	perpendicular distance of thrust line below center of gravity, ft
$F_x$	x component of total aerodynamic force in the trajectory axis system, lb (appendix A)
$F_z$	z component of total aerodynamic force in the trajectory axis system, lb
$F(s)$	filter transfer function
$g$	acceleration due to gravity, 32.2 ft/sec <sup>2</sup>
$\dot{h}_b$	reference sink rate for glide-slope extension, ft/sec
$h_e$	altitude error from glide-slope beam center, ft
$h_f$	initiation altitude of the feedback control law in the flare, ft
$\dot{h}_f$	desired vertical touchdown velocity, ft/sec
$\dot{h}_0$	sink rate at touchdown, ft/sec
$h_r$	reference altitude for the flare law, ft
$h_{\text{ramp}}$	altitude at which the predictive pitch ramp command begins, ft
$h_{\text{step}}$	altitude at which the predictive pitch step command begins, ft
ILS	instrument landing system, standard radio guidance installed at major airports
$I_{YY}$	aircraft moment of inertia around y-axis, slug-ft <sup>2</sup>

$i_T$	thrust angle of incidence with body respect to x-axis (up, positive), radians
$k$	filter gain constants
$k_\epsilon$	glide-slope tracking gain constant
$L$	aerodynamic lift force, lb
$L_u, L_w$	horizontal and vertical turbulence scale lengths, respectively, ft
$m$	airplane mass, slugs
$n$	number of observations in a statistical sample
$n_{\dot{h}}$	percentage of $\dot{h}$ feedback as compared to $\ddot{h}$ feedback in the flare law
$n_x$	x-component of gust in earth axis
$n_z$	z-component of gust in earth axis
$q$	pitch angular velocity, radians/sec
$R_u(r), R_w(r)$	spatial autocorrelation function of the longitudinal and vertical components of turbulence, respectively
$S$	wing reference area, ft <sup>2</sup>
$s$	Laplace transform operator
$s^2$	sample variance
$T$	total thrust, lb
$t$	sampling time interval, sec
$V$	airspeed, ft/sec unless otherwise indicated
$V_c$	velocity command, ft/sec
$v_I$	velocity of the aircraft with respect to the inertial frame of reference, ft/sec
$v_{xg}$	x-component of total wind in earth axis, ft/sec
$\bar{v}_{xg}$	x-component of mean wind in the earth axis system, ft/sec
$v_{zg}$	z-component of total wind in earth axis, ft/sec
$\bar{v}_{zg}$	z-component of mean wind in the earth axis system, ft/sec
$v_i$	



$x_0$	horizontal distance of aircraft at touchdown from the ground intercept of the ILS glide-slope beam (touchdown distance)
$z$	$z$ transform operator
$()_{GE}$	ground effect
$\alpha$	angle of attack, radians
$\gamma$	flight-path angle, radians
$\gamma_{ILS}$	ILS glide path angle, radians
$\delta_e$	elevator deflection, radians
$\delta_f$	flap deflection, radians
$\epsilon$	glide-slope error angle, radians
$\epsilon_c$	capture initiation angle, radians
$\eta$	angle between body axis and trajectory axis of the aircraft
$\theta$	pitch angle of airplane body axis relative to horizon, radians
$\mu$	sample mean
$\rho$	air density, slugs/ft <sup>3</sup>
$\sigma$	standard deviation of the quantity denoted by the subscript
$\Phi(\Omega), \Phi(\omega)$	spatial and temporal power spectral density of the turbulence
$\Omega$	spatial frequency of the gusts, radians/ft
$\omega$	angular frequency, radians/sec

#### Subscripts

c	command signal
d	desired quantity
i	input, or initialization quantity
o	output, or quantity at touchdown

$T$	component tangential to the flight path
$u, v$	longitudinal and vertical components of the quantity
$(\bar{\phantom{x}})$	average
$1, 2$	first and second runs of a paired observation

# INVESTIGATION OF A DIGITAL AUTOMATIC AIRCRAFT LANDING SYSTEM IN TURBULENCE

Frank Neuman and John D. Foster

Ames Research Center

## SUMMARY

A digital system has been studied for automatically controlling the longitudinal motion of a large transport aircraft during the landing phase. The study was carried out by means of an all-digital simulation that was chiefly concerned with investigating the effects of gusts and wind shears on aircraft control near the ground. The performance of the automatic control system operating in turbulence was determined by a Monte Carlo technique.

With respect to the digital control system, it was found that (1) the basic analog flare mode could be modified to improve its performance under conditions of turbulence and wind shear; (2) for most control modes the computation rate requirement is surprisingly low, as indicated by the effects of computer repetition rate on the aircraft performance; (3) the performance degradation that results when a control computation cycle is occasionally skipped is relatively minor, a fact that is significant when the computer is shared with other systems for which emergency computations may have to be performed.

Some of the causes of hard touchdowns showed the feasibility of developing a more efficient Monte Carlo technique that would aid future investigations.

## INTRODUCTION

Recent history of aviation has seen a continuing trend toward automation. Most current transport aircraft are equipped with analog automatic control systems that are used routinely during the cruise phase and can be coupled to the ILS beam for portions of the approach. Systems have now been developed that will permit automatic control of aircraft to touchdown. Although research aircraft use these systems for landing under zero visibility conditions, for commercial operation there is still concern for the accuracy of the guidance information, the reliability of the automatic systems, and the effectiveness of situation information displays necessary for recovery from malfunctions.

This investigation was undertaken because it was believed that digital control techniques could contribute to the objective of achieving acceptable automatic landings under all operational conditions. Four specific contributions were identified: (1) Combining many functions in a computer relieves the pilot from secondary manual tasks now associated with automatic landing operations. The ultimate goal would be for the pilot to become a decision-making systems' manager rather than a primary control element. (2) Data stored in the computer are available for selective or

automatic call and observation by the pilot. This flexibility is also important in a research environment where one attempts to define the type and form of the data needed by the pilot in his new role as systems' manager. (3) Digital computations are repeatable precisely. Since redundant systems are required for safety, several computers making calculations based on identical sensor data must produce identical answers. Failure to do so is an instant warning of malfunction. (4) More sophisticated control laws can be implemented that will improve performance at a small cost of computer storage and computation time.

While digital control has been used extensively in military aircraft, the economic factor has so far prevented its commercial application. However, since transport aircraft projected for the future will have a substantial on-board digital computer capability for other purposes for which analog computations are unsatisfactory (such as navigation computations, fuel management, and engine performance monitoring), economics will no longer be a deterrent.

Flight control requirements for commercial jet transports differ significantly from those of military aircraft. It is therefore appropriate to examine digital control problems specifically for commercial jet transport aircraft. A primary requirement is extreme safety. One aspect of flight safety is system reliability. Another aspect is the effect of the environment such as noisy guidance information and wind turbulence. System reliability has been studied extensively and various techniques, such as component redundancy and self-checking, have been investigated in depth. It has been shown in reference 1 that turbulence causes larger deviations from the desired flight path than the errors in ILS guidance. This study therefore concentrated on the effect of turbulence on safe automatic landings.

The present study had three specific objectives. The first was to choose an efficient method of translating analog autopilot technology directly into digital control laws to take advantage of previous experience in analog autopilot design. This was a desirable step before considering improved designs which take advantage of the superior logical capability of the digital machine. The second objective was to study some improvements of an analog flare law. This goal was easily accomplished in the digital system but would have been difficult to implement in an analog system. The third, and main objective of the study, was to determine the influence of wind turbulence on the performance of the automatic control system during landing. The very nonlinear problem of flare and touchdown was attacked by Monte Carlo methods. If primary attention had been focused on the approach phase, which can be effectively expressed by a linear model, the more efficient power spectral method with gaussian noise, described in reference 1, could have been used.

In line with the above objectives, a digital method was developed to generate the turbulent wind components. Since the method has wide application, it is described in detail in the body of the report.

For this investigation, the scope of the automatic landing problem was restricted in two ways. First, the jet transport simulation equations reported in reference 2 were reduced to three degrees of freedom by considering the longitudinal axis only. This restriction is reasonable in light of the accident statistics compiled in reference 1 which concludes that accidents due to longitudinal errors are fatal much more often than accidents due to lateral errors. Second, the system guidance information was assumed to come from an error free ILS beam and altimeter.

## SIMULATION OF THE AUTOMATIC LANDING SYSTEM

In this section the longitudinal automatic landing system will be described, and some of the design considerations will be given. The system is illustrated by combinations of flow charts and block diagrams that indicate its digital nature and its analog heritage. Reference 3 is an excellent discussion of linear analog aircraft control laws. Additional information of modern autopilot design was obtained by private communication from the author of reference 4. While linear filters will be described by transfer functions, it should be understood that the filtering function is actually performed in the digital computer by solving difference equations. This process is described in appendix B.

### Mode Controller

The flight control laws are segmented into control modes for different portions of the approach and landing. A mode controller automatically selects the proper control mode in sequence (i.e., the altitude hold, glide-slope capture, glide-slope tracking, and flare mode) according to predetermined criteria. In accordance with conventional practice (ref. 4), the control modes operate on the velocity and pitch-stabilized aircraft (see fig. 1), and therefore operate with only three command variables, velocity command  $V_c$ , pitch angle command  $\theta_c$ , and flap command  $\delta_{fc}$ . Data on the basic airplane and design of the inner stabilization loop are contained in appendix A.

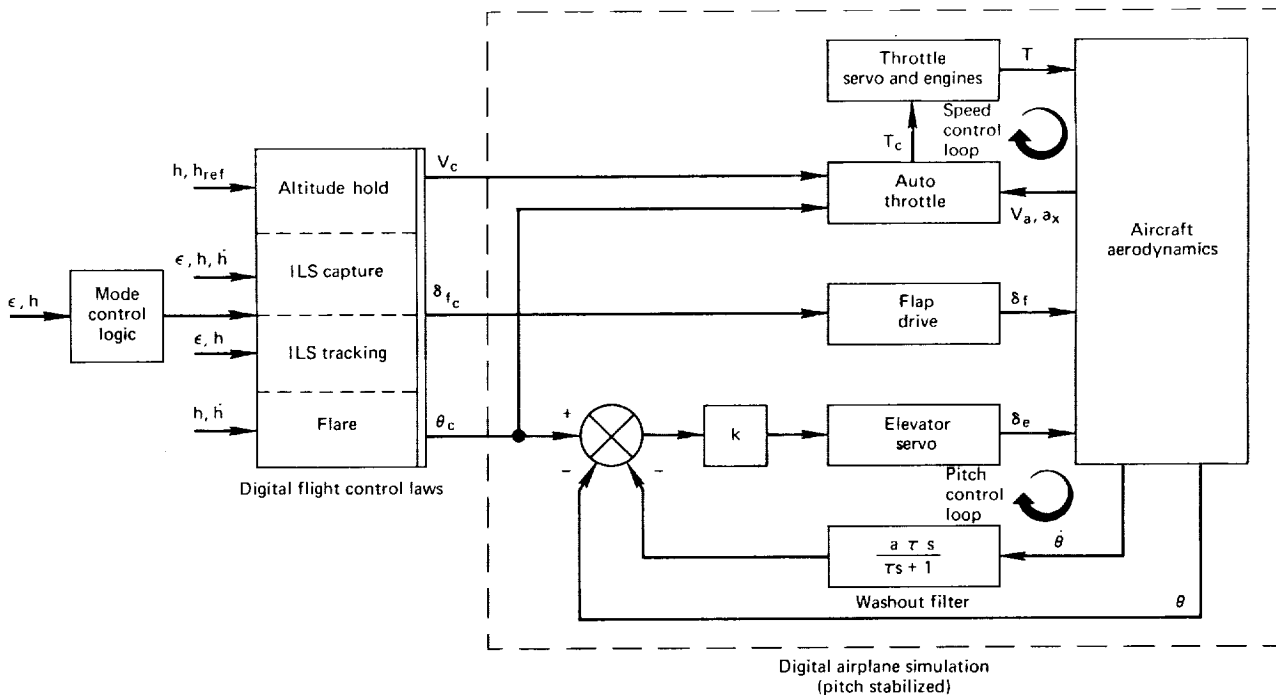


Figure 1.— Overall block diagram of the simulation.

The operation of the mode controller is shown in the form of a Fortran flow chart in figure 2. While the controller selects from only four modes, it passes through six different conditions. Conditions 1 and 4 are preparatory to actual mode switching.

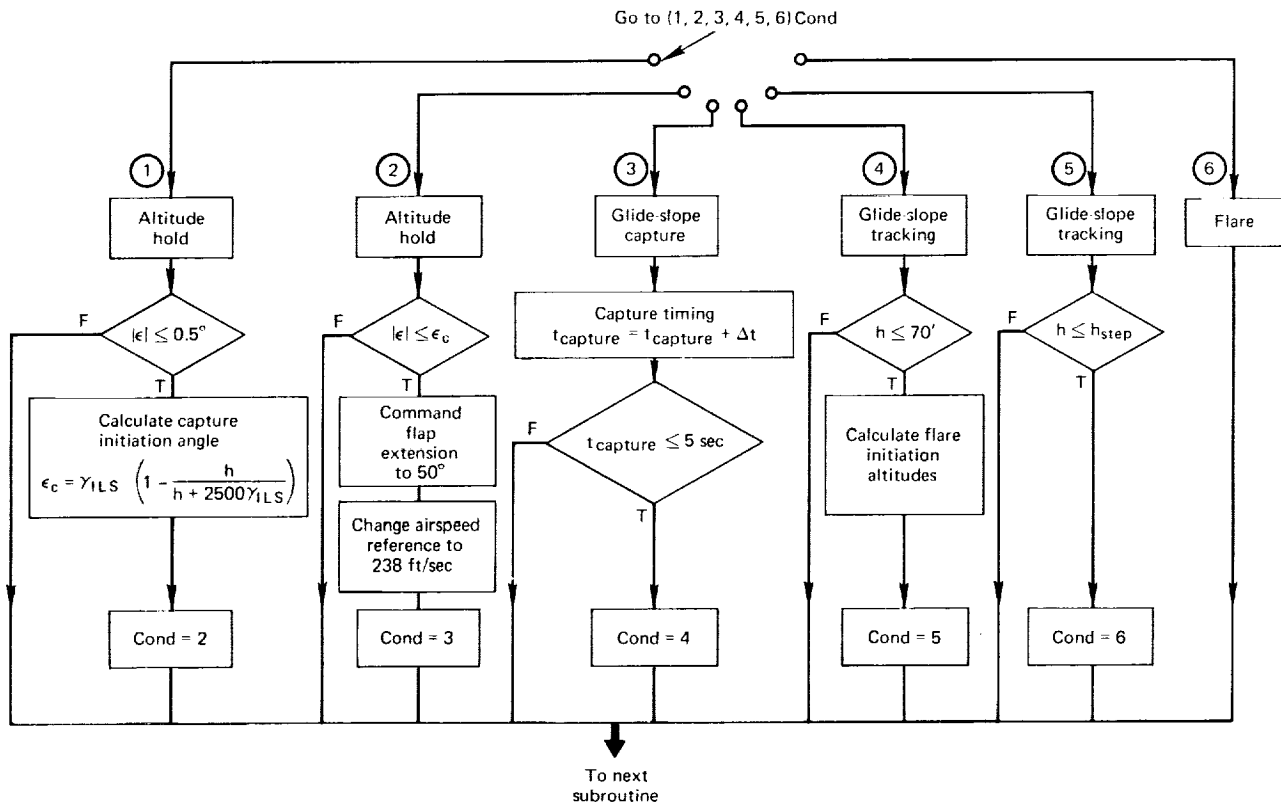


Figure 2.— Mode control logic.

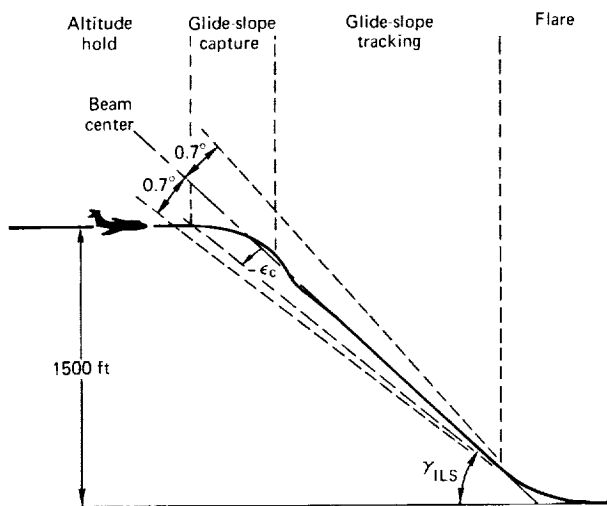


Figure 3.— Automatic landing geometry using ILS and radar altimeter.

The mode controller is best described by considering a landing approach (see fig. 3). The aircraft approaches the ILS glide slope at a constant altitude of 1500 feet (condition 1, fig. 3). It penetrates the beam until the glide-slope error angle detected by the ILS receiver is equal to or less than  $0.5^\circ$ . At this point the capture initiation angle  $\epsilon_c$  is calculated from the aircraft altitude  $h$  and the glide-slope angle  $\gamma_{ILS}$ .

$$\epsilon_c = \gamma_{ILS} \left[ (1 - h) / (h + 2500 \gamma_{ILS}) \right]$$

The mode controller then goes to condition 2 until  $\epsilon_c$  is reached. This permits the initiation of capture at the same distance from the beam center (2500 ft) independent of aircraft altitude. At this point the flaps are

commanded to extend to 50° and the controller switches to the capture mode. The capture mode, condition 3, is timed and switched to glide-slope tracking, condition 4, after 5 seconds. Glide-slope tracking proceeds to a preselected altitude, at which point the sink rate and velocity of the aircraft are used to calculate the flare initiation altitude  $h_{\text{step}}$  and other initiation parameters described in the flare mode section. The mode controller is then switched to condition 5 and glide-slope tracking is continued until  $h_{\text{step}}$  is reached, at which point the flare mode is selected.

Notice that no automatic go-around mode is provided. The simulated aircraft is forced to land so that the conditions can be found that result in unsatisfactory landings.

### Detailed Description of the Control Modes

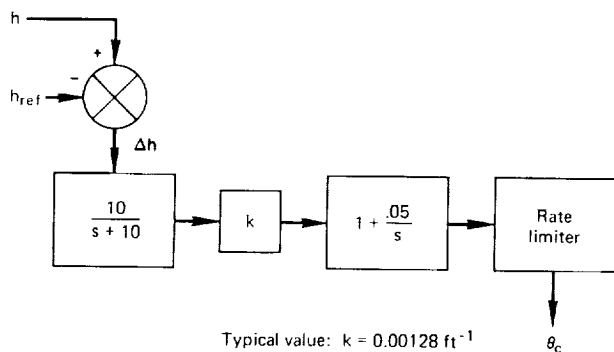


Figure 4.— Altitude hold mode.

$$\Delta h = h - h_{\text{ref}}$$

$$\theta_c = c_1 \theta_{c-1} + c_2 \theta_{c-2} + c_3 \Delta h + c_4 \Delta h_{-1}$$

These equations are solved once each computation cycle.

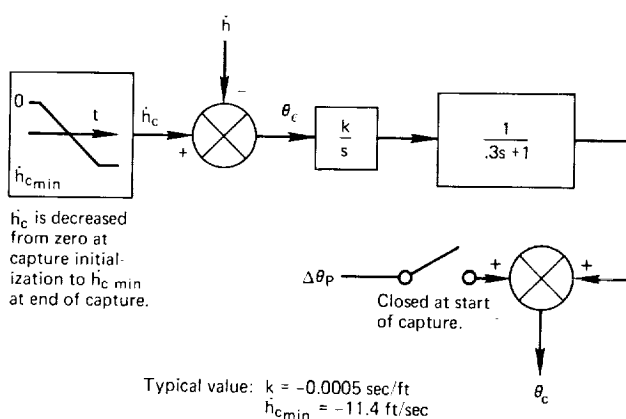


Figure 5.— Capture mode.

*Altitude hold mode*— A simple altitude hold mode incorporated in the system provides the initial conditions for capture. The digital control was modeled after the representative analog system shown in figure 4. The system consists of a differencing circuit for calculating the altitude error  $h$ , followed in series by a low pass filter, a gain, and a low gain integrator. For comparison, the digital equivalent equations are as follows (see eq. (8) table 8):

*Capture mode*— The capture mode (fig. 5) provides for a smooth rotation from level flight to the glide-slope angle. This mode, specifically designed for this digital simulation, differs from capture modes used in analog systems in that a small step pitch angle command  $\Delta \theta_p$  is applied at capture initiation to rotate the airplane. The magnitude of the step is based on the glide-slope angle of the beam to be captured. In addition, an inertial vertical velocity error signal is generated to increase the sink rate linearly from capture initiation to the proper sink rate for the given glide-slope angle and velocity command. The pitch error signal  $\theta_e$  is

then integrated and filtered to produce the pitch angle command. The integrator provides an error signal proportional to altitude error. Since the sink rate reference is a ramp function whose final value is the proper sink rate of the aircraft on the glide slope, the resulting altitude reference is a parabolic curve that smoothly intersects the glide slope. As shown in the mode control logic at the beginning of capture the flaps are deployed from  $35^\circ$  to  $50^\circ$ , causing a smooth reduction of airspeed.

*Glide-slope tracking mode*— After glide-slope capture the aircraft remains in the glide-slope tracking mode until flare. The glide-slope error angle  $\epsilon$  is filtered as shown in figure 6. The tracking loop operates on both the error and the integral of the error. Its gain is adjusted proportional to the altitude from capture to 200 feet. Reducing the gain with decreasing altitude will correct signal output approximately in proportion to displacement of aircraft from the beam center instead of in proportion to angular displacement measured by  $\epsilon$ . Because of various signal reflections in the region close to the ground, the path becomes so irregular that it is difficult to follow. Therefore, the above gain reduction is insufficient and  $k_\epsilon$  is smoothly reduced to zero between 200 and 100 feet altitude. In air turbulence the aircraft tends to wander around the glide-slope center, occasionally experiencing large sink rates. These are a problem only at altitudes below 200 feet where it is important to keep the sink rate close to its proper value so that the flare mode can safely land the aircraft. Therefore, a glide-slope extension signal added to the tracking signal damps the tracking response below 200 feet and eventually controls the aircraft to a constant sink rate regardless of its glide-slope position. This extension is a pitch attitude command  $\theta_c$ , proportional to  $\dot{h} - \dot{h}_b$ , where  $\dot{h}_b$  is the proper sink rate for the given glide slope.

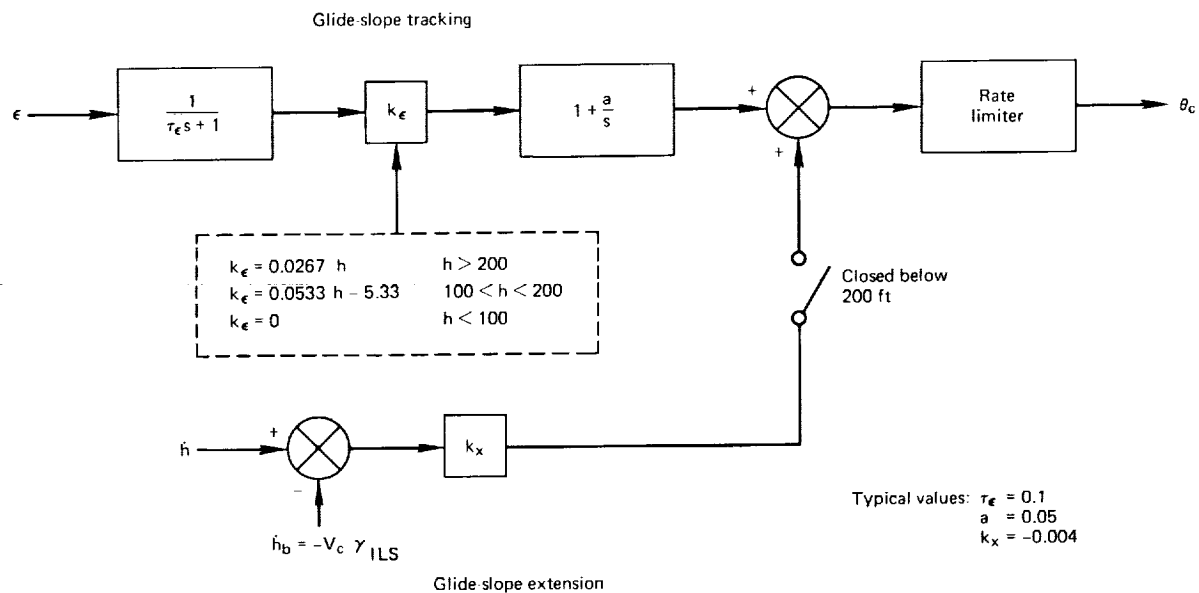


Figure 6.— Glide-slope tracking mode.



*Flare mode*— The flare mode controls the traditional exponential flare (ref. 4). The flare has three boundary conditions:

$h_f$  initiation altitude of the feedback control law

$\dot{h}_f$  initial sink rate

$\dot{h}_{fo}$  desired vertical touchdown velocity (taken as 1.5 ft/sec for this simulation)

A flare law that satisfies these boundary conditions is:

$$h_R(t) = (h_f - a_2 \dot{h}_{fo}) e^{-t/a_2} + a_2 \dot{h}_{fo} \quad (1)$$

and  $a_2$  is calculated as

$$a_2 = -h_f / (\dot{h}_f - \dot{h}_{fo}) \quad (1a)$$

The reference sink rate is the derivative of equation (1)

$$\dot{h}_R = -(1/a_2) (h_f - a_2 \dot{h}_{fo}) e^{-t/a_2} \quad (2)$$

The predictive portion of the flare law (fig. 7) has two sections, a step command in pitch,  $\Delta\theta_p$ , which causes the aircraft to begin to rotate, and a ramp pitch command  $\Delta\theta_R$ , which begins somewhat later. With no other disturbance, the predictive flare commands will generate an approximately exponential flare. Feedback is used to overcome disturbances. Equation (1) is the solution of the following differential equation:

$$\ddot{h}_R + a_2 (\dot{h}_R + \dot{h}_{fo}) \quad (3)$$

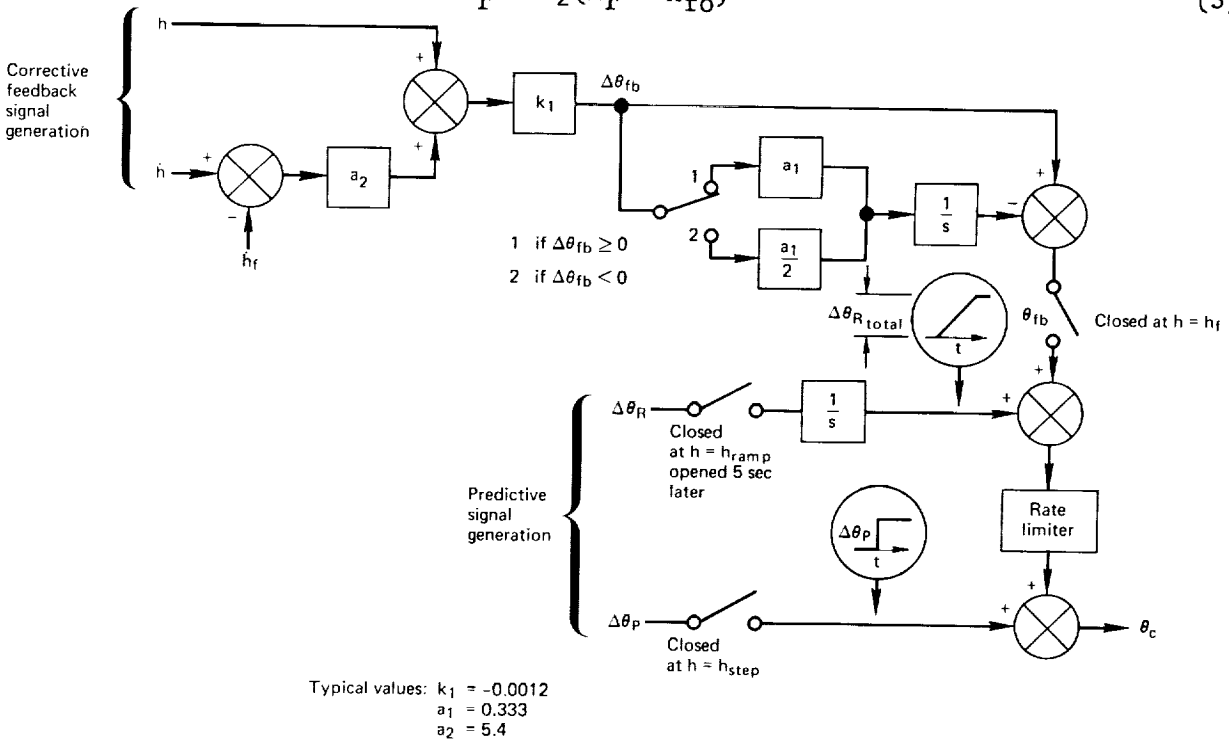


Figure 7.— Flare mode block diagram.

with the boundary conditions  $h_r = h_f$  at  $t = 0$  and  $\dot{h}_r = \dot{h}_{f0}$  at  $h = 0$ . The feedback portion of the flare law generates a corrective signal when equation (3) is not fulfilled by the actual altitude  $h$  and sink rate  $\dot{h}$  in place of  $h_r$  and  $\dot{h}_r$ . The corrective signal is (see fig. 7):

$$\theta_{fb} = k_f [1 + (a_1/s)] [h + a_2 (\dot{h} - \dot{h}_f)] \quad (4)$$

which is added to the predictive pitch command. Hence, no correction signal is applied when the reference path is followed.

There is, however, a difference between the flare laws implemented on modern analog automatic landing systems and the flare law implemented here. In many modern analog systems the predictive pitch commands as well as the feedback gain constants and the flare initiation altitude  $h_f$  are preselected for the nominal glide-slope angle. In our digital system these values are computed from the flight-path angle  $\gamma$  just before flare initiation. This method stabilizes the landing performance when the flight path is disturbed by windshear or turbulence.

The flare law used in this investigation is shown in detail in the form of a Fortran flow chart in figure 8. When the flare subroutine is entered for the first time, the sink rate is used to calculate decision altitudes for the predictive flare law commands. The altitude at which these initial calculations are made is somewhat above the highest at which the flare may be started. As figure 8

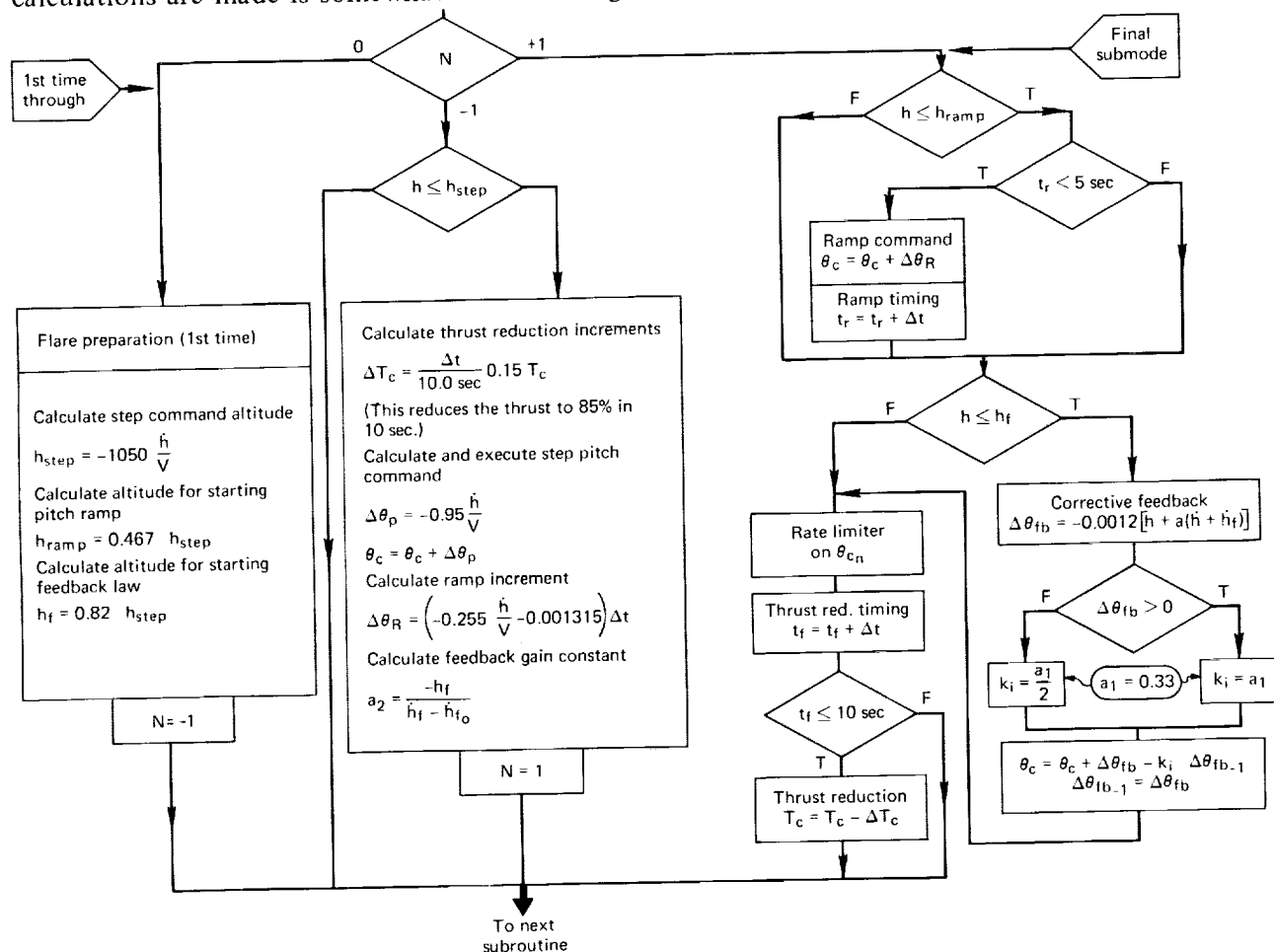


Figure 8.— Fortran flow chart of flare computations.

shows, the step command altitude is proportional to the flight-path angle  $\gamma \cong -\dot{h}/V$ . The ramp begins at a proportionally lower altitude. Since the aircraft does not begin to deviate from a straight-line glide path instantaneously upon receiving the pitch step command, the altitude for the corrective feedback to begin is also selected proportionally lower than the step command altitude. After these calculations are completed, the flare computer transfers the authority back to the glide-slope tracking control.

When the step command altitude,  $h_{\text{step}}$ , is reached, the flare control mode takes over completely. First a thrust reduction  $\Delta T_C$  is calculated and from the latest measured sink rate,  $\dot{h}$ , the step command  $\Delta\theta_P$  is calculated and executed. Then the ramp increment  $\Delta\theta_R$  and the feedback gain constant  $a_2$  are calculated. At this point the flare computer is switched to its final submode.

In the final submode the predictive ramp pitch command is added to the corrective feedback flare command. The summed signals are transmitted as the pitch change command  $\theta_C$  to the pitch control loop of the aircraft. In addition, a timed thrust reduction is programmed to reduce the speed at touchdown.

Some features of the flare mode of figure 6 were incorporated because of the simulation and flight-test results of a flare system reported in reference 5. In that system (1) command rate limiting was used, (2) the corrective feedback integrator gain was positive for pitch-up commands only and zero for pitch-down commands, and (3) the total pitch command could never be smaller than the initial pitch command. The first two features added to the present flare law improved the performance by reducing touchdown velocities and thus were incorporated in the final simulation. The best rate limiter was found to be 0.0926 radian per second. The best integrator gains were achieved when the pitch-down gain was half the pitch-up gain. The third feature did not improve performance so was not used.

Under disturbances, the feedback term in the flare law (eq. (4)) does not attempt to guide along a path fixed in space, or even hold  $h(t)$  and  $\dot{h}(t)$  at given values. As long as the feedback signal of equation (4) is zero no correction is made. Disturbances, therefore, tend to cause translations of the touchdown point rather than large maneuvers to meet a given touchdown point which would often cause hard landings.

With the above remarks in mind, an improvement in the predictive flare command was made, which is not shown in figures 6 and 7. Instead of a timed ramp signal, the total increase in pitch command due to the ramp was applied between the ramp initiation altitude ( $h_{\text{ramp}}$ ) and ground as a function of change in altitude between computation cycles,  $h_n - h_{n-1}$ . Thus the change in pitch command for each cycle is computed as:

$$\Delta\theta = \left( \Delta\theta_{\text{rtotal}} / h_{\text{ramp}} \right) (h_n - h_{n-1})$$

This change replaces the timed ramp increments. Thus, when wind shear causes a fast drop in altitude, the predictive pitch command is applied at a faster rate, while the total change  $\Delta\theta_{\text{rtotal}}$  remains constant.

Another measurable variable  $\ddot{h}$  often available from aircraft sensors might improve the flare performance of the airplane. A differential equation that contains  $\ddot{h}$  and that also has equation (1) as a solution is

$$\ddot{h} + n_h^* a_2 \dot{h} - (1 - n_h^*) a_2^2 \ddot{h} - a_2 h_f = 0 \quad (5)$$

where  $n_h^*$  is a factor between 0 and 1, and  $n_h^* = 1$  results in the previously described feedback signal of equation (4). If vertical acceleration is measured, equation (5) with properly chosen  $n_h^*$  may provide the corrective signal that will improve performance under turbulent conditions.

## REPRESENTATION OF ATMOSPHERIC TURBULENCE FOR AIRPLANE SIMULATION

### Background

Before presenting the analysis and results of this study, it is important that the atmospheric turbulence model be understood, because it has a major effect on the experimental results. The following section therefore presents the mathematical development of the digital turbulence model.

Turbulence has three velocity components. For the pitch axis control problem only the longitudinal and vertical gust components  $u_g$  and  $w_g$  are of concern. Both are functions of both time and position. Figure 9 shows that the measured turbulence records obtained from an aircraft will be different for different flight speeds over the same flight path. Therefore, the spatial spectra calculated from the flight records will be different. Also, because of the limited sample time, the measured spectra differ from the actual spectra. For reasonable flight speeds, the changes in  $u_g$  and  $w_g$  are smaller with respect to time than with respect to position. Therefore, for purposes of calculation, the gust velocity vectors at each point will be assumed not to vary with time. This is the concept of the turbulence field frozen with respect to time. Then, as figure 10 shows, the time records for two flights at different but constant speeds will be similar to each other and to the

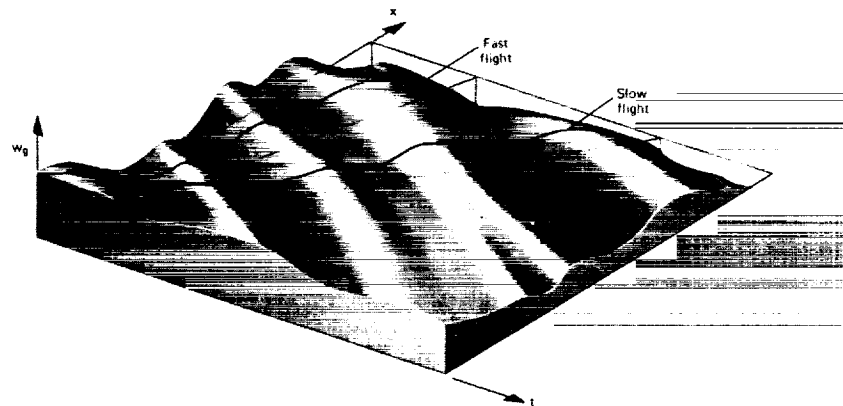


Figure 9.— Time and position history of vertical turbulence.

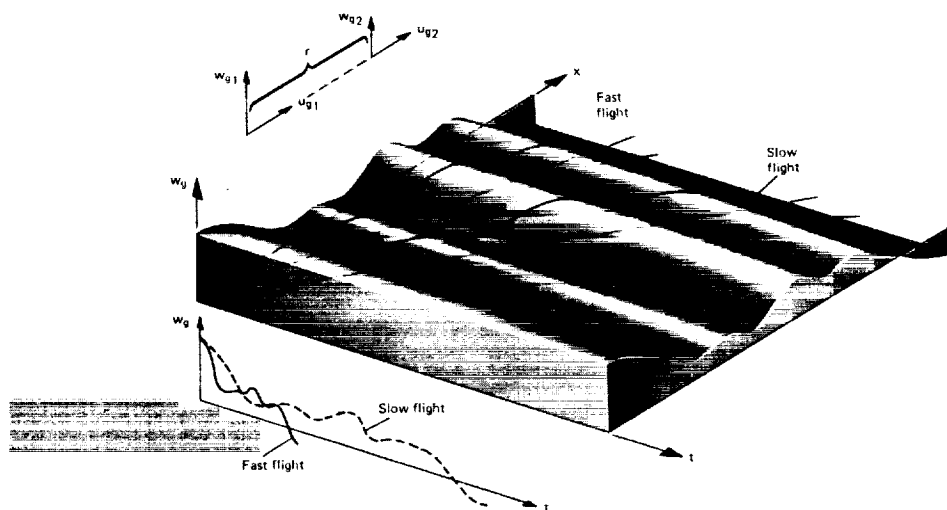


Figure 10.— Frozen gust pattern of  $\omega_g$ .

spatial distribution. If the flight speed is known at all times, even if it is varying, the time record can be converted to a spatial record of turbulent velocity components. To obtain the parameters of the mathematical model of turbulence, the spatial records are then fitted to the theoretical power spectra.

A particular set of power spectra, the Dryden spectra (ref. 6), is easy to simulate and shows reasonable agreement with measured spectra and was therefore selected for this simulation. For the Dryden spectra one chooses the longitudinal spatial autocorrelation function of gust velocity to be a simple exponential (see ref. 5)

$$R_u(r) = \sigma_u^2 e^{-r/L_u} \quad (6)$$

From the equation of continuity, Batchelor (ref. 7) has shown that the longitudinal and vertical autocorrelation functions are related by the equation

$$R_w(r) = R_u(r) + \frac{r}{2} \frac{\partial R_u(r)}{\partial r} \quad (7)$$

Therefore, since for homogeneous turbulence  $\sigma_u = \sigma_w$ ,  $L_u = L_w$ ,

$$R_w(r) = \sigma_w^2 \left( 1 - \frac{r}{2L_w} \right) e^{-r/L_w} \quad (8)$$

The one-dimensional spatial power density spectra are obtained by substitution of equations (6) and (8) into the well-known relation

$$\phi(\Omega) = \frac{2}{\pi} \int_0^{\infty} R(r) \cos(\Omega r) dr \quad (9)$$

resulting in

$$\left. \begin{aligned} \phi_u(\Omega) &= \sigma_u^2 \frac{2L_u}{\pi} \frac{1}{1 + L_u^2 \Omega^2} \\ \phi_w(\Omega) &= \sigma_w^2 \frac{L_w}{\pi} \frac{1 + 3L_w^2 \Omega^2}{(1 + L_w^2 \Omega^2)^2} \end{aligned} \right\} \quad (10)$$

In these and the following equations

- L scale length, ft
- $\Omega$  spatial frequency, rad/ft
- $\omega$  angular frequency, rad/sec
- V aircraft ground speed, ft/sec
- $\sigma$  root-mean-square value of turbulence velocity, ft/sec, standard deviation
- r correlation interval, ft

It is also assumed that the horizontal and vertical power spectra are uncorrelated.

The actual turbulence depends on the two parameters L and  $\sigma$ . Insufficient data exist to define L and  $\sigma$  for all conditions. In the interim the following relationships will be used.

$$\left. \begin{aligned} \sigma_u &= 0.2 \bar{u}_g \\ \sigma_w &= 0.2 \bar{u}_g (0.5 + 0.00098 h) \quad 0 \leq h \leq 500 \text{ ft} \\ \sigma_w &= 0.2 \bar{u}_g \quad h > 500 \text{ ft} \end{aligned} \right\} \quad (11)$$

where  $\bar{u}_g$  is the mean longitudinal wind velocity and h is the altitude above ground. Also the horizontal gust scale length is much less affected by altitude than is the vertical scale length.

$$\left. \begin{aligned} L_u &= 100 \sqrt[3]{h} \quad h > 230 \text{ ft} \\ L_u &= 600 \quad h \leq 230 \text{ ft} \\ L_w &= h \end{aligned} \right\} \quad (11a)$$

In general, turbulence increases with mean wind. Because of the effect of the ground there is also an increase of vertical gust component with altitude (ref. 8, fig. 4) while the mean wind and

horizontal gust component are independent of altitude. These relationships apply for approach altitudes up to 2000 feet, which are considered in this report. Thus, on the ground, wing altitude is 10 feet,  $L_u$  is 600 feet, and  $L_w$  is 10 feet, but they are equal at 1000 feet.

It should be noted at this point that the relationships for  $L_u$ ,  $L_w$ ,  $\sigma_u$ , and  $\sigma_w$  are not consistent with the assumption of homogeneous turbulence. However, it is assumed throughout the literature that using homogeneous equations with different values for the horizontal and vertical parameters provides a more realistic description of turbulence.

### Simulation

For simulation purposes the spatial spectra are converted to temporal frequency spectra, which are a function of  $V$ , the aircraft velocity (ref. 5),

$$\Phi(\omega) = \frac{1}{V} \Phi(\Omega) \quad (12)$$

Using equation (12), and noting that  $\Omega = \omega/V$ , equations (10) become

$$\Phi_u(\omega) = \left( \frac{L_u}{V} \right) \frac{2\sigma_u^2}{\pi} \frac{1}{1 + (L_u/V)^2 \omega^2} \quad (13)$$

$$\Phi_w(\omega) = \left( \frac{L_w}{V} \right) \frac{\sigma_w^2}{\pi} \frac{1 + 3(L_w/V)^2 \omega^2}{[1 + (L_w/V)^2 \omega^2]^2} \quad (14)$$

The above equations are defined so that

$$\int_0^{\infty} \Phi(\omega) d\omega = \sigma^2$$

for equations (13) and (14). Note that the frequency spectra throughout this section are defined for positive frequencies only.

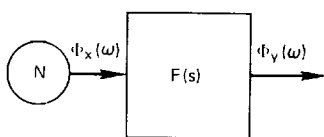


Figure 11.— Power spectrum shaping.

For simulation it is necessary to generate turbulence with the required spectrum  $\Phi(\omega)$  of standard deviation  $\sigma$  and scale length  $L$  for a given flight velocity and altitude. A wide band noise  $\Phi_X(\omega)$  is thus applied to a linear filter of the proper frequency response to obtain  $\Phi_Y(\omega)$  (see fig. 11). In order to carry out this operation, first find the filter transfer function  $F(s)$ . The relation of input to output power spectrum is

$$\Phi_Y(\omega) = |F(s)|_{s=j\omega}^2 \Phi_X(\omega) \quad (15)$$

If the input power spectrum is white noise  $\Phi_X(\omega) = 1$ , then

$$\Phi_Y(\omega) = |F(s)|_{s=j\omega}^2 \quad (16)$$

Now define

$$\left. \begin{aligned} a_u &= \frac{V}{L_u} ; & k_u &= \frac{2a_u\sigma_u^2}{\pi} \\ a_w &= \frac{V}{L_w} ; & b &= \frac{V}{\sqrt{3} L_w} ; & k_w &= \frac{3a_w\sigma_w^2}{\pi} \end{aligned} \right\} \quad (17)$$

In conjunction with equation (16), equations (13) and (14) become

$$|F_u(j\omega)|^2 = \frac{k_u}{\omega^2 + a_u^2} \quad |F_w(j\omega)|^2 = \frac{k_w(\omega^2 + b^2)}{(\omega^2 + a_w^2)^2}$$

which results in

$$F_u(j\omega) = \frac{\sqrt{k_u}}{j\omega + a_u} \quad F_w(j\omega) = \frac{\sqrt{k_w}(j\omega + b)}{(j\omega + a_w)^2}$$

Finally for

$$F_u(s) = \frac{\sqrt{k_u}}{s + a_u} \quad (18a)$$

$$F_w(s) = \frac{\sqrt{k_w}(s + b)}{(s + a_w)^2} \quad (18b)$$

*Digital simulation equations*— Since the noise is to be generated digitally, one must supply a digital equivalent of random gaussian noise and either write the differential equations from the transfer functions and solve them by numerical integration, or develop difference equations that approximate the filters. The filters of equations (18a) and (18b) were simulated by means of difference equations, since this is an efficient method of computation. The principles used to generate the difference equations are discussed in appendix B. From table 8 and equation (18b), the difference equation for the vertical spectrum is

$$y_n = C_1 y_{n-1} - C_2 y_{n-2} + D_1 x_{n-1} + D_2 x_{n-2} \quad (19)$$

where the constants of equation (19) are

$$C_1 = 2e^{-a_w T} \quad (20)$$

$$C_2 = -e^{-2a_w T} \quad (21)$$

$$D_1 = \sqrt{k_w} \left[ \frac{b}{a_w^2} + e^{-a_w T} \left( \frac{a_w - b}{a_w} T - \frac{b}{a_w^2} \right) \right] \quad (22)$$

$$D_2 = \sqrt{k_w} \left[ \frac{b}{a_w^2} (e^{-a_w T} - 1) - \frac{a_w - b}{a_w} T \right] e^{-a_w T} \quad (23)$$



The difference equation for the horizontal spectrum described by equation (18a) is

$$y_n = Cy_{n-1} + Dx_{n-1} \quad (24)$$

where the constants of equation (24) are

$$C = e^{-a_u T} \quad (25)$$

$$D = \frac{\sqrt{k_u} (1 - e^{-a_u T})}{a_u} \quad (26)$$

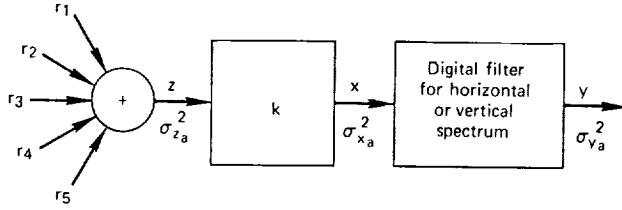


Figure 12.— Digital simulation of turbulent gust.

The filter input is a gaussian random sequence (see fig. 12). A good approximation of the wide band gaussian noise input sequence is provided by summing five pseudo random numbers ( $r_j$ ) with a flat distribution in the range  $-1$  to  $+1$  (see, e.g., ref. 9)

$$z_i = \sum_{j=1}^5 r_{ji} \quad \sigma_z^2 = \frac{5}{3}$$

and adjusting the variance of the sequence to generate the proper output variance by selecting the multiplication factor  $k$  ( $x_i = kz_i$ ,  $\sigma_x^2 = k^2 \sigma_z^2$ ). For this purpose the ratios of actual output to input variance  $\sigma_y^2 / \sigma_x^2$  of the filters in figure 12 must be found. A good approximation for small  $T$  has been calculated for both filters in appendix C:

$$\frac{\sigma_y^2}{\sigma_x^2} = \frac{T}{\pi} \sigma_y^2 \quad (27)$$

where  $\sigma_y^2$  is the desired and  $\sigma_x^2$  the actual output variance of equation (13) or (14). Hence, to generate the desired output variance,  $\sigma_y^2 = \sigma_y^2$ , the variance of the input sequence,  $\sigma_x^2$ , must be  $\sigma_x^2 = \pi/T$ . This is achieved by premultiplying each  $z_i$  by the factor  $k$  to give  $x_i$ ,

$$k = \sqrt{\frac{\pi}{T \sigma_z^2}} \quad (28)$$

For efficient calculations the constant  $k$  of equation (28) is combined with the input coefficients  $D_j$  of the difference equations (19) and (24).

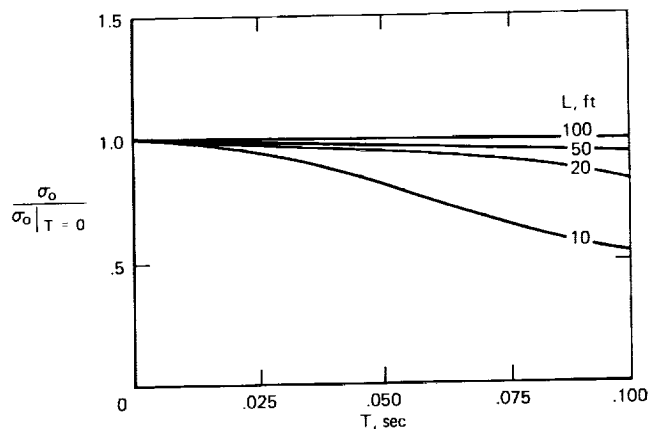


Figure 13.— Reduction of output variance of the vertical power spectrum with increase in sample time interval ( $V = 220$  ft/sec).

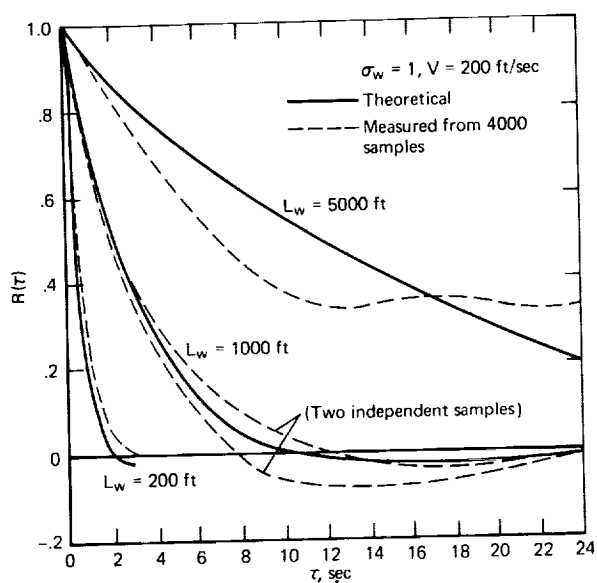


Figure 14.— Autocorrelation of the vertical gust spectra.

$$\sigma_{\Delta u_g}^2 = \overline{[u_g(x-r) - u_g(r)]^2} = 2[\sigma_u^2 - R_u(r)] \quad (29)$$

and from equation (6)

$$\sigma_{\Delta u_g}^2 = 2\sigma_{u_g}^2(1 - e^{-r/L_u}) \quad (30)$$

*Properties of the turbulence model*— Figure 13 shows the reduction in output variance due to increasing  $T$  as calculated from the exact equation in appendix C. The reduction is greatest for short scale lengths (low altitudes) and long sampling intervals because the high-frequency components are not presented. However, since the rigid aircraft does not respond to high frequencies, the absence of them does not affect the results of the simulation.

To verify that the digital turbulence simulation behaved as predicted from the Dryden spectra model, 4000 noise samples for different scale lengths ( $L = 200, 1000, 5000$ ) for  $t = 0.1$  sec were generated and the autocorrelations calculated. The autocorrelation functions of the limited samples agreed well with the theoretical prediction (see fig. 14). The adequacy of generating noise samples at 0.1 sec intervals was verified by statistical runs made with the simulated aircraft at  $t = 0.025$  sec and at  $t = 0.1$  sec, the value normally used in this simulation, and no significant difference in systems performance was found.

An important property of the turbulence is the change in turbulent velocity,  $\Delta u_g$ , over a given distance  $r$  because such changes affect the flight path of the airplane. This gradient property for the longitudinal Dryden spectrum has been derived in reference 10 for a random initial value. Since  $u_g$  is gaussian, so is  $\Delta u_g$  by symmetry with a mean of zero. The variance of  $\Delta u_g$  is

Equations (29) and (8) can be used to derive the gradient properties of the vertical gust component,

$$\sigma_{\Delta w_g}^2 = 2\sigma_w^2 \left\{ 1 - [1 - (r/2L_w)]e^{-r/L_w} \right\} \quad (31)$$

The gradient properties of the simulated horizontal turbulence were checked for a 2,000,000-foot sample with airspeed and scale length typical of landing and a variance of 16. The cumulative distributions  $\Delta u_g$  at various separations  $r$  for  $L_u = 100$  to  $L_u = 1000$  feet were plotted on normal probability graph paper (not shown) and the measured gradients agreed well with the theoretically predicted gradients.

In summary, for the digital simulation, equations (11) and (11a) were applied to calculate the turbulence parameters as functions of altitude and average wind velocity. These parameters were then taken to calculate the difference equation coefficients (eqs. (20)-(23), (25), (26)) whenever the altitude of the aircraft changed. Finally, a gaussian random sequence of  $x_g$ 's (fig. 12) of the proper variance (eq. (27)) was generated and inserted into the difference equations (19) and (24) to calculate the vertical and longitudinal gust components,  $y_n$ .

## TECHNIQUES FOR ANALYZING THE SIMULATED FLIGHTS

### Statistical Analysis

Under turbulent conditions, system performance has to be measured statistically. While it is possible to measure errors for each control mode, performance indexes were established only for the glide-slope tracking mode and the flare mode, because they were the major influence on the automatic landing performance. Information given in the section on results indicates that the altitude hold and capture modes performed satisfactorily.

The glide-slope tracking mode provides the proper initial conditions for the flare mode. To track correctly, the airplane must remain well within the beam, except during glide-slope extension. The ability to remain within the beam was measured by two criteria. The first measured the mean and standard deviation of the altitude error from the center of the ILS beam,  $\bar{h}_e$ ,  $\sigma_{\bar{h}_e}$ . These values were calculated for each flight from the end of capture to the beginning of the flare. The altitude error instead of the glide-slope angle error was chosen as a guidance measure even though the guidance signal is proportional to the glide-slope angle because the other choice would have weighted path errors close to flare very heavily. The second criterion, which also measured the ability to remain within the ILS glide-slope beam, was taken from an FAA advisory circular (ref. 11), which deals with automatic-pilot-coupler systems used as part of a category II installation. It requires system performance criteria to be met under the following wind conditions: a downwind component of 10 knots and, commencing at an altitude of 500 feet, a wind shear of 4 knots per 100 feet altitude. To provide satisfactory glide-slope performance the criterion requires that the aircraft be stabilized on the glide slope before reaching an altitude of 700 feet above the field level. From 700 feet altitude to the decision altitude the autopilot-coupler should cause the airplane to track the center of the indicated glide slope to within  $\pm 35$  microamperes or  $\pm 12$  feet, whichever is the larger, without sustained oscillations. Notice that the criterion compensates for the increased position error sensitivity at low altitudes by changing from an angular error

( $150 \mu A = 0.7^\circ$ ) to an altitude error. While the criterion is apparently to be applied only for the windshear condition stated, it was applied to all simulated flights in this investigation, and the percentage outside the above limits was calculated.

For a successful flare, reasonable initial conditions must be established. As a measure of these conditions, which are the terminal conditions of the glide-slope tracking, the airplane flight variables were recorded at 75 feet altitude, and for each series of flights the mean and variance of the parameters were calculated. Only the significant parameters for a successful flare will be discussed.

For the flare performance only the sink rate at touchdown,  $\dot{h}_0$ , and touchdown distance from the glide slope to ground intersection,  $x_0$ , are calculated. Since we are not actually controlling for minimum deviation from a desired flight path, mean squared flight-path error was not calculated for the flare.

Landing point dispersions caused by the flare control law can be separated from those caused by horizontal position errors at flare initiation. Since the flare law does not operate on horizontal position errors, the variance of the landing distance from glide slope ground intercept is the sum of the flare law induced errors and the flare window position errors. We define the flare window position error as the aircraft position error from the glide-slope position at 75 feet altitude. Computer time is saved because it is possible to initialize the aircraft on the glide slope at an altitude of 200 feet when one intends to study effects of altering the flare law. Starting the system from 45,000 feet out results in the flare window position error, which is characteristic of the overall landing system. Starting at an altitude of 200 feet on the glide slope (3800 ft from glide slope intercept) results in a smaller flare window position error. If the smaller flare window position error is subtracted from the touchdown position error and the characteristic flare window position error for the overall system is added, the proper overall touchdown dispersion is

$$\sigma_{x_0}^2 \Big|_{x_i=45,000} = \sigma_{x_0}^2 \Big|_{x_i=3,800} + \left( \sigma_x^2 \Big|_{\substack{h=75 \\ x_i=45,000}} - \sigma_x^2 \Big|_{\substack{h=75 \\ x_i=3,800}} \right)$$

The effects of altitude errors were insignificant, since starting the aircraft simulation from 200 ft altitude introduced sufficient attitude dispersion at the 75-foot altitude. An example is given using data for the case of 20 feet head wind.

$$\sigma_{x_0}^2 \Big|_{x_i=45,000} = (540)^2 + [(120)^2 - (81)^2] = (546)^2$$

As one can see, the effect of neglecting the second term would be rather small.

For flights without turbulence only one flight was necessary for each condition since the digital computer repeated identical flights exactly. In turbulence at least 100 flights were simulated for each of seven different values of gust variance. For each series of flights the mean and standard deviations of all the performance measures were calculated (e.g.,  $\bar{h}_e$ ,  $\sigma_{\bar{h}_e}$ ).

## Paired Observations

When a comparison is made between two slightly different control laws in an actual noisy environment, the variation of the noise may mask the difference in control law performance, and many flights must be made to achieve a valid comparison. In a digital simulation the noise in a pair of flights can be matched exactly with different control laws. Therefore, it is possible to apply statistical tests with sets of paired observations. The variation in performance for each pair due to turbulence variations is eliminated, which makes detection of performance differences easier. The variation in the turbulence for different pairs causes variations in the landing performance but only differences in performance due to different control laws are measured. The difference in the measured quantities for each pair of flights constitutes one observation, for example,

$$y = \dot{h}_{O1} - \dot{h}_{O2}$$

As usual, in testing the hypothesis that there is no difference in performance for the two control laws one applies Student's t-test and calculates  $t$  (see, e.g., ref. 12)

$$t = \frac{\bar{y}}{\sqrt{s^2/n}} ; \quad s^2 = \frac{\sum_1^n y^2 - [(\sum y)^2/n]}{n - 1} , \quad \bar{y} = \frac{1}{n} \sum_1^n y$$

where  $n$  is the number of observations. For  $n=100$  the critical regions are  $t > 1.9840$  and  $t < -1.9840$ . When the resulting  $t$  is in one of the critical regions, we can say that with 97.5 percent probability one of the systems performs better with respect to the variable  $y$ . Which system, of course, is determined by the specific critical region, and the best estimate of the average improvement is  $\bar{y}$ .

## AUTOMATIC CONTROL SYSTEM PERFORMANCE

### Comparison of Analog and Digital Control System Performance

The basic digital control system was compared with an equivalent analog system. It is well known that the performance of a sample-data system becomes equal to that of an analog system as the sample interval goes to zero. Therefore, instead of developing a complete analog simulation including the aircraft equations of motion, the digital program was written in such a manner that the sample time interval could be made arbitrarily small. By reducing the interval from 0.1 second (the interval used for most data runs) to 0.01 second, it was established that there were no significant differences in performance in calm or turbulent conditions. Few runs were needed, even in turbulence, since runs could be compared in matched pairs. The matched pairs were derived from solutions to the aircraft equations and stability augmentation equations, and from the turbulence samples at intervals of 0.01 second. Only the control computation cycle time was changed. Figure 15 shows a comparison of simulation flights. Since the turbulence is a function of altitude and time, slight variations in the flight path before the flare will change the turbulence encountered during the flare; and since the flare is sensitive to the exact form of the turbulence, the same turbulence is required for matched flights. The runs were, therefore, re-initialized at an altitude of

200 feet. The flight paths were slightly different as would be expected from the difference in time intervals for control command changes. Statistically, however, there was no performance difference between the quasi-continuous and the digital system.

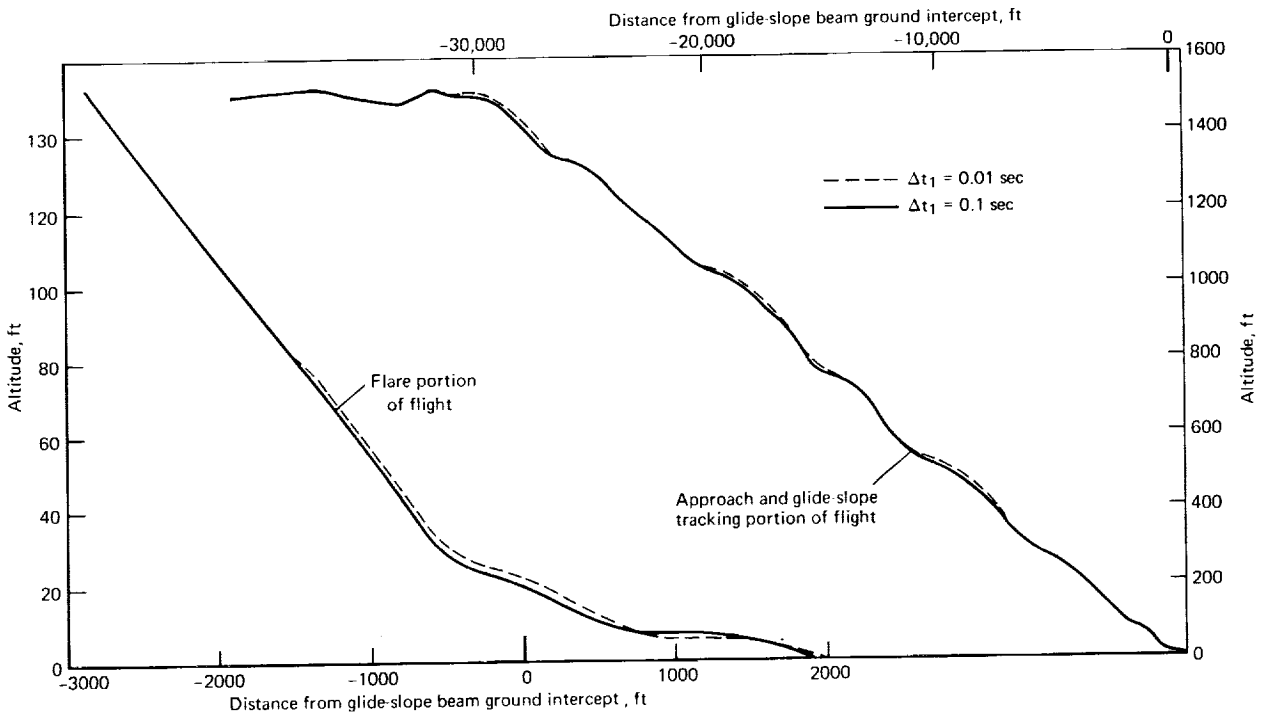


Figure 15.— Matched pair of flights in 20 ft/sec, headwind with turbulence.

### Performance of the Noncritical Control Modes

In a comparison of the performance differences due to various modifications of the autopilot, the comparison must be made for each control mode separately. The altitude hold mode and the glide-slope capture mode were not altered after the first design since they performed satisfactorily under all conditions and they have the least influence on the final criterion for a successful landing. The flight paths in figure 16 for different glide-slope angles under no wind conditions illustrate the operation of these modes. Note the smooth glide-slope capture, with hardly any overshoots. The flight paths in the altitude hold mode, under no wind conditions, are simply straight horizontal lines. The glide-slope intercept altitudes were changed only to simplify the figure and are not intended to suggest deviation from the standard 1500-foot approach. Figure 17 shows short sections of flights in turbulence for the altitude hold mode followed by the capture maneuver. Twenty flight paths are superimposed for each turbulent condition to show the widening of the flight envelope with increase in turbulence. Since low pitch rates are important for passenger comfort, the pitch command was limited to  $2.5^\circ$  per second in the altitude hold mode, but a rate limit was not imposed during the capture mode. Although not shown, simulation of the altitude hold mode with and without this limiter did not indicate any significant difference in flight paths.

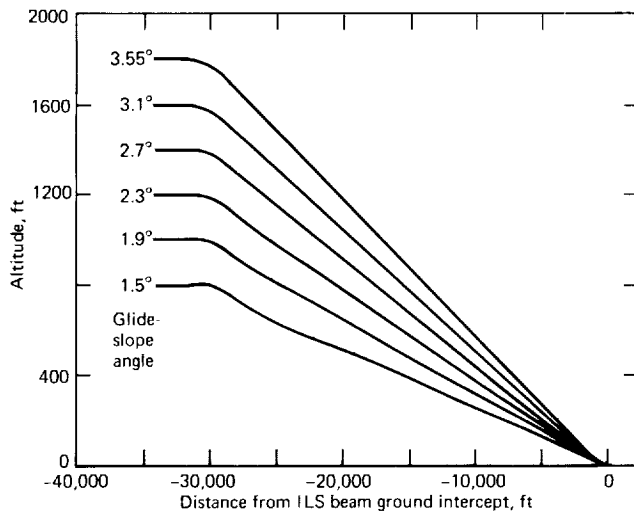


Figure 16.— Glide-slope capture for different glide-slope angles.

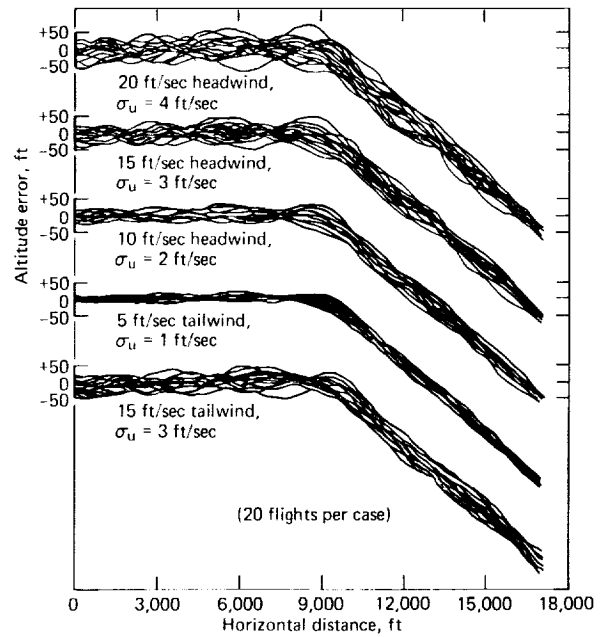


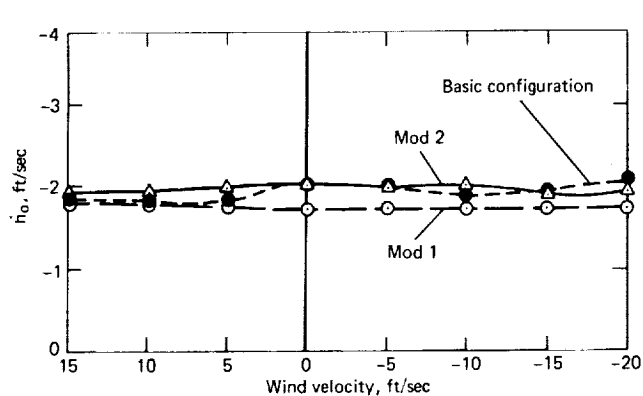
Figure 17.— 3° glide-slope capture in turbulence.

#### Performance of the Critical Control Modes Under Steady Wind Conditions and Simple Shear

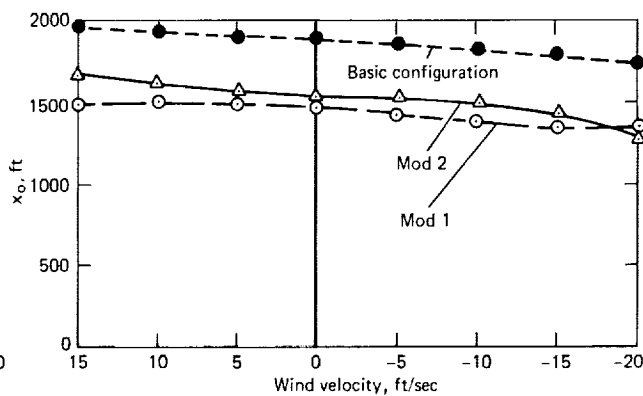
Three configurations of the flare law were tested in steady winds with and without wind shear. In the first configuration (basic flare law), the predictive pitch command ramp (fig. 7) was applied as a function of time. The first modification was a pitch ramp based on altitude change that occurred in each sampling interval. The total pitch angle change was a predetermined constant. The second modification was the same as the first, except that vertical acceleration feedback was added. In the tests, the simulation was begun at an altitude of 1500 feet about 9 miles from the runway in the automatic altitude hold mode. The wind velocity was varied between tests in increments of 5 ft/sec, from a head wind of 20 ft/sec to a tail wind of 15 ft/sec. For the flights with a wind shear, a constant shear of 4 knots/100 ft was used. In all cases, with wind shear, the ground wind was zero.

Steady winds had no significant effect on the performance of the altitude-hold, glide-slope capture, and glide-slope tracking modes. For the three flare modes,  $\dot{h}_0$ , the sink rate at touchdown and  $x_0$ , the horizontal distance from the glide slope at touchdown, were not significantly affected by steady wind, but  $x_0$  was reduced for the modified flare laws (figs. 18(a) and 18(b)).

In the presence of wind shear, the landing performance of the three flare laws was similar to that without shear, but varied more with wind speed (figs. 19(a) and 19(b)). There was no significant effect on  $\dot{h}_0$ , and the modified flare laws were superior for control of  $x_0$ , resulting in a 350-foot shorter landing distance.

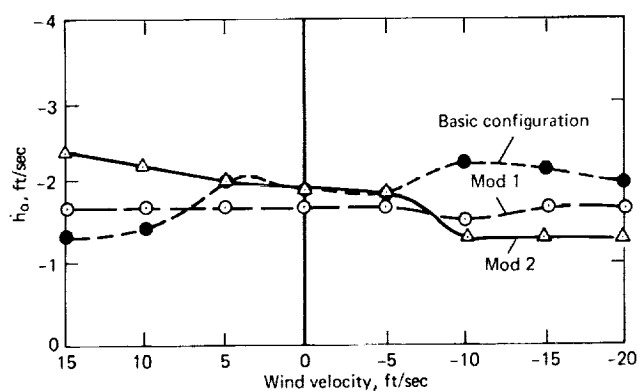


(a) Sink rate at touchdown vs. wind velocity; no wind shear.

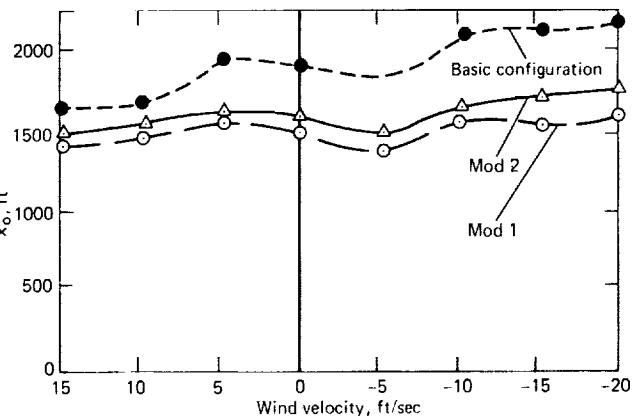


(b) Horizontal distance from glide-slope beam center at touchdown vs. wind velocity; no wind shear.

Figure 18.— Flare performance in the presence of steady wind.



(a) Sink rate at touchdown vs. wind velocity; with wind shear of 4 knots/400 ft.



(b) Horizontal distance from glide-slope beam center at touchdown vs. wind velocity with wind shear of 4 knots/100 ft.

Figure 19.— Flare performance in the presence of wind shear.



## Performance of the Critical Control Modes Under Turbulent Conditions

The ultimate test of a system is its performance under the influence of natural disturbances. For the landing performance there is no one-to-one relation between the performance under steady conditions, as described in the last section, and performance under turbulent conditions.

*Glide-slope tracking*— Table 1 shows the performance of the glide-slope tracking mode over a range of different wind conditions, where

$\overline{\Delta x}$       average position error from the ideal position at 75 feet altitude on a 3° glide slope  
(x(actual) – x(ideal))

$\bar{h}_e$       average glide-slope tracking error (positive is above beam center)

$\sigma_{\bar{h}_e}$       glide-slope tracking error standard deviation

The simulation was initiated 45,000 feet from glide slope to ground intercept, and the above variables were calculated while the glide-slope tracking mode was engaged.

TABLE 1.— GLIDE-SLOPE TRACKING PERFORMANCE (100 RUNS PER CONDITION)

Wind	$\sigma_{u_g}$	$\dot{h} _{h=75\text{ft}}$	$\sigma_{\dot{h}} _{h=75\text{ft}}$	$\overline{\Delta x} _{h=75\text{ft}}$	$\sigma_{\overline{\Delta x}} _{h=75\text{ft}}$	$\bar{h}_e$	$\sigma_{\bar{h}_e}$	Percent outside FAA limit
-20	4	10.97	1.60	52	120	-0.463	13.1	12.0
-15	3	10.92	1.20	25	110	-.526	10.03	3.9
-10	2	11.07	.93	7	69	-.962	6.90	.6
-5	1	11.07	.55	8	36	-1.55	3.72	0
5	1	11.64	.47	-61	37	.76	3.56	0
10	2	11.23	.91	-130	64	.70	6.6	0
15	3	12.20	1.20	-197	86	1.29	9.3	4.9

Examination of table 1 will disclose the following facts. The average glide-slope tracking error is slightly negative for head winds, which means that the airplane remains below the glide slope most of the time. The reverse is true for tail winds. The standard deviation of the tracking error increases with the standard deviation of the turbulence, as has already been shown qualitatively in figure 17. The average sink rate at 75 feet altitude is smallest for the weakest head wind and largest for the strongest tail wind because of the constant airspeed command of 230 ft/sec. The standard deviation of the sink rate at the flare window,  $\sigma_{\dot{h}}$ , is relatively small, and shows the expected trend of increase for turbulence. The percentage of flight time that the flight path was outside the limit specified in reference 11 is also shown. An on-board calculation of this error could be used to measure the severity of the turbulence, which would determine whether or not to continue with the automatic approach. The average position error  $\overline{\Delta x}$  at 75 feet altitude follows the trend predicted from the average altitude error. It is, however, somewhat larger than would be predicted from the

altitude error along the glide slope alone. Here it must be remembered that the glide-slope tracking control begins to switch over to a sink rate control law below 200 feet altitude, and at 100 feet altitude no attempt is made to correct for beam tracking errors. Again, the standard deviation of the position errors at the flare window is largest for the greatest turbulence.

The accuracy of achieving the flare window with the glide-slope extension was measured for a 20 ft/sec head wind in turbulence. Without glide-slope extension the standard deviation of the rate of descent at 75 feet increased from 1.6 to 3.1 ft/sec, and the position error standard deviation increased from 120 to 260 feet.

*Flare mode*— As discussed earlier, the flare maneuver is the most critical one for successful touchdowns in turbulence. For this reason various modifications to the flare control mode were studied. Table 2 summarizes the results for the more important changes investigated, each row summarizing a set of 100 touchdowns; the turbulence samples were matched for all flights, so that each set of flights could be compared to another set by means of the t-test described earlier. The table is subdivided into five groups according to the modifications investigated. This organization requires repetition of the data for some of the experiments, see column 2.

A detailed explanation of the conditions for each experiment will be presented after some preliminary remarks about the significance of the data in some selected columns. Columns 1 to 5 present experimental conditions and columns 6 to 16 present experimental results. The small tables at the bottom of the figure present statistical test results of comparing pairs of runs for sink rates, touchdown distances, and pitch at touchdown. The results are listed in table 3 with their standard deviations.

The third parameter of importance in landings, the pitch angle at touchdown,  $\theta_0$ , and its standard deviation, will be discussed only briefly since, in all cases, the pitch angles were in the safe range to prevent a tail strike of the airplane. It is interesting that the differences in average pitch angle, although small, are statistically significant for many of the experiments. An examination of the raw data for each pair of flights showed that sign reversals in the term  $\theta_{01} - \theta_{02}$  were less frequent than sign reversals for  $h_{01} - h_{02}$  and  $x_{01} - x_{02}$ . For the vertical touchdown velocity our greatest interest is in the tail of the distribution, since it includes the cases of hard landings, which must be prevented. Therefore, a touchdown velocity frequency table, columns 14–16, is included for each experiment.

The rows of table 2 present only a summary of the simulation results. The set of runs labeled Experiment 1 was the final "best system" selected after investigating various control law modifications. It will be noted that Experiment 1 is compared with other experiments for all except the first comparison, which was made to determine a control law configuration that was subsequently incorporated into the final system. Each subsequent comparison, tests 2-5, shows the effects of changing the control law from its configuration for Experiment 1. In all cases the sink rate increases for a modification although sometimes not to a statistically significant degree. It would be generally desirable to have a short touchdown distance to leave adequate roll out distance on the runway. Low sink rate at touchdown and short touchdown distance are not naturally compatible; but since sink rate is considered to be more important, the best configuration chosen was a compromise weighted more heavily toward low sink rates.

TABLE 2.— COMPARISON OF CONTROL LAW MODIFICATIONS WHEN FLYING IN SEVERE TURBULENCE ( $\sigma_u = 7.0$  FT/SEC)

	1	2	3	4	5	6	7	8	9	10	11	12	13	14	15	16
No.	Flare law modification comparison tests	Experiment no. (100 runs per experiment)	$n_h$ per unit $h$ feedback (see eq. (6))	Ratio of pitch down to pitch up integrator gain	Pitch command rate limit, deg/sec	$h_o$ no wind, ft/sec	$h_o$ , ft/sec	$\sigma_h$ , ft/sec	$x_o$ no wind, ft	$x_o$ , ft	$\sigma_{x_o}$ , ft	$\theta_o$ , rad	$\sigma_{\theta_o}$ , rad	Touchdown velocity frequency table		
	Soft landing 0-4 ft/sec													Hard landing 4-8 ft/sec	Landing gear damage 8-10 ft/sec	
1	Standard flare vs flare with calculated flare altitude and $h$ dependent ramp	8	1.0	0.5	5	2.0	3.58	1.7	1900	833 720	0.045	0.0069	67	31	2	
		3	1.0	.5	5	1.76	3.06	1.4	1495	1338 620	.053	.01	75	24	1	
2	Different pitch up and pitch down integrator gains	4	.9	1.0	5	1.65	3.14	1.5	1169	716 460				78	21	1
		1	.9	.5	5	2.02	2.87	1.4	1560	1003 630	.050	.0096	83	17	0	
3	$h$ feedback effects	3	1.0	.5	5	1.76	3.06	1.4	1495	1338 620	.053	.01	75	24	1	
		1	.9	.5	5	2.02	2.87	1.4	1560	1003 630	.050	.0096	83	17	0	
4	Rate limit comparison	2	.85	.5	5	1.42	3.17	1.6	1595	885 660	.047	.01	75	22	3	
		5	.9	.5	2.5	2.02	3.09	1.6	1560	964 630	.049	.0093	78	21	1	
5	Best flare compared to best flare with constant flare altitude	1	.9	.5	5	1.02	2.87	1.4	1560	1003 630	.050	.0096	83	17	0	
		6	.9	.5	$\infty$	2.02	2.92	1.3	1560	1059 640	.050	.0097	82	18	0	
6		1	.9	.5	5		2.87	1.4	1560	1003 630	.050	.0096	83	17	0	
		7	.9	.5	5	1.02	3.01	1.4	1560	1093 730	.049	.0095	82	18	0	

Student's T-test results:

Run no.	1	2	3	4	5	6	7	8
1	X	S	N	S	S	N	N	
2	S	X	N					S
3	S	S	X					
4	S			X				
5	N				X	N		
6	S					S	X	
7	S							X
8			S					X

Sink rate,  $h_o$

Pitch at touchdown

Touchdown distance,  $x_o$

S Statistically significant difference at the 0.995 significance level  
 S- Statistically significant difference at the 0.975 significance level  
 N No statistically significant difference

The capability of selecting flare altitude and other flare parameters from the sink rate of the aircraft (Exp. 3) rather than having standard flare parameters (Exp. 8) was the first control improvement that was investigated. The average sink rate at touchdown was decreased by 0.52 ft/sec and, as the frequency table shows, the variance was reduced by having fewer high sink rate touchdowns at the cost of adding distance to touchdown. It should be noted, however, that reducing the variation in touchdown distance resulted in better performance overall. For all further tests the sink rate dependent flare feature of Experiment 3 was incorporated in the final system.

The second control modification studied was providing smaller integrator gain for pitch down than for pitch up; see column 4. The effect of this modification with otherwise the "best" flare law (Exp. 1) is shown in section 2. The trend is similar to that for the first control law modification discussed. The average sink rate decreases and the average touchdown distance increases.

The third control law modification studied was the effect of vertical acceleration feedback (column 3). A comparison of the sink rates for the best vertical acceleration feedback,  $n_h = 0.9$ , and no acceleration feedback,  $n_h = 1.0$ , showed no statistically significant difference. Moreover, any difference would be of little practical interest, since the minimum is not very pronounced. An increase in vertical acceleration feedback ( $n_h$  changing from 1.0 to 0.85) does decrease the average touchdown distance, while only slightly increasing its standard deviation. As a compromise,  $n_h = 0.9$  was chosen.

Pitch command rate limiting is required for passenger comfort. Since the flare maneuver requires greater pitch command activity, a pitch command rate limit of  $5^\circ$  per second was chosen, which is twice the limit of the pitch command rate for the glide-slope tracking mode. As can be seen from table 2, section 4, it was desirable to increase the rate limit, column 5. When the rate limit was completely removed (Exp. 6), the only statistically significant difference that occurred was an increase in touchdown distance.

There is an inherent danger in the piecemeal improvement of a complicated system. If one optimizes one parameter and introduces additional control parameters, there is no assurance that the first parameter's optimum adjustment will be optimum for the new system. Therefore, a final experiment was made (shown also in table 2, section 5), which proved that indeed there was a small advantage in computing the flare altitude, rather than preselecting it from the nominal glide-slope angle and approach speed, when otherwise the various improvements were kept. The improvement due to this portion of the flare law is not so clear cut as it was when it was first added to the analog equivalent system.

A large sample of data for the 30 ft/sec head wind was taken in seven sections of 100 flights each and is represented in table 3. The purpose was to examine the variability between data runs with identical statistical turbulence, and to study the cause of high sink rate landings. The listing for each experiment of 100 runs includes a frequency table of the sink rates at touchdown. The last four lines of the table present the average of the seven runs, their standard deviation, the standard deviation divided by the average of each column, to show the relative variation of each column, and the probability distribution for the sink rate. In the touchdown sink rate frequency table, the  $\sigma/\mu$  data indicate that the center of the distribution is pretty well defined. However, the tails of the high sink rate distribution are not sufficiently well defined even with 700 individual flight records. For the design of actual flight systems, this lack of information would be serious, since we

are mainly interested in the number of hard landings that we can expect. It will also be noticed that the standard deviations of gust velocity  $\sigma_{u_g} = (\sum \sigma_{u_{g1}}^2 / 100)^{1/2}$  averaged over each of the 100 flights are lower than would be expected from the gust model  $\sigma_{u_g} = 0.2\bar{u}_g = 6$  ft/sec ( $\sigma_{u_{g1}}^2$  is the variance of the gust about the mean for each particular run). This difference comes from the fact that for the given spectrum shape the average variance of a short sample is smaller than the variance of an infinite sample (see, e.g., ref. 12, fig. 3).

TABLE 3.— DATA SUMMARY FOR SEVEN EXPERIMENTS OF 100 RUNS EACH IN SEVERE TURBULENCE (30 FT/SEC HEAD WIND,  $\sigma_u = 6$  FT/SEC)

Experiment number	$\sigma_{u_g}^2$	$\bar{h}_0$ no wind	$\bar{h}_0$	$\sigma_{h_0}$	$x_0$ no wind	$\bar{x}_0$	$\sigma_{x_0}$	No. of touchdowns within indicated sink rate limits, ft/sec											
								0-1	1-2	2-3	3-4	4-5	5-6	6-7	7-8	8-9	9-10	10-11	
1	4.54	2.02	3.09	1.3	1560	1666	630	4	21	23	25	20	5	1	1	0	0	0	
2	4.46	↓	2.84	1.0	↓	1516	540	4	18	36	29	12	0	0	1	0	↓	↓	
3	4.50		3.12	1.4		1600	580	5	14	33	27	12	5	2	0	2			
4	4.61		2.91	1.2		1660	590	4	21	31	27	12	1	4	0	0			
5	4.43		2.86	1.2		1558	600	3	23	34	23	13	2	2	0	0			
6	4.68		3.10	1.3		1521	620	4	20	30	22	12	10	1	1	0			
7	4.62		2.89	1.3		1620	470	5	23	28	26	10	5	2	1	0			
$\mu$	4.55			2.97		1.24		1592	566.6	4.14	20	30.7	25.6	13.0	4.0	1.71			0.57
$\sigma$	0.0917		0.124	0.127		61.8	54.2	0.69	3.1	4.3	2.4	3.2	3.3	1.2	0.53	0.756	0	0	
$\sigma/\mu$	0.02		0.042	0.102		0.038	0.096	0.16	0.15	0.14	0.095	0.247	0.84	0.73	0.93	2.64	---	---	
$P(h_0/\sigma_u = 6 \text{ ft/sec}) = \mu/100$								0.0414	0.2	0.307	0.256	0.13	0.04	0.017	0.0057	0.00286	---	---	

We primarily want to know the major cause of hard landings. In the simulation it is easy to separate the effects of the vertical and horizontal gust components. One simply compares three sets of flights: one with both gust components present, one with vertical gust removed, and one with horizontal gust removed. As shown in table 4, the sink rate at touchdown was significantly smaller for the vertical gusts alone. Also, the dispersion of the sink rate at touchdown was decreased by a factor of 2. This indicates that for the assumed turbulence model horizontal gusts have a major effect on the sink rate. The horizontal gust patterns are shown in figure 20 for 17 flights with high

TABLE 4.— EFFECT OF GUST COMPONENTS ON LANDING PERFORMANCE  
[25 flights each at 20 ft/sec head wind]

Gust components present	$\bar{h}$	$\sigma_{\bar{h}}$	$\bar{x}_0$	$\sigma_{\bar{x}_0}$
Both components	-2.4	1.2	1015	580
Horizontal only	-2.5	.99	857	460
Vertical only	-1.6	.44	901	310

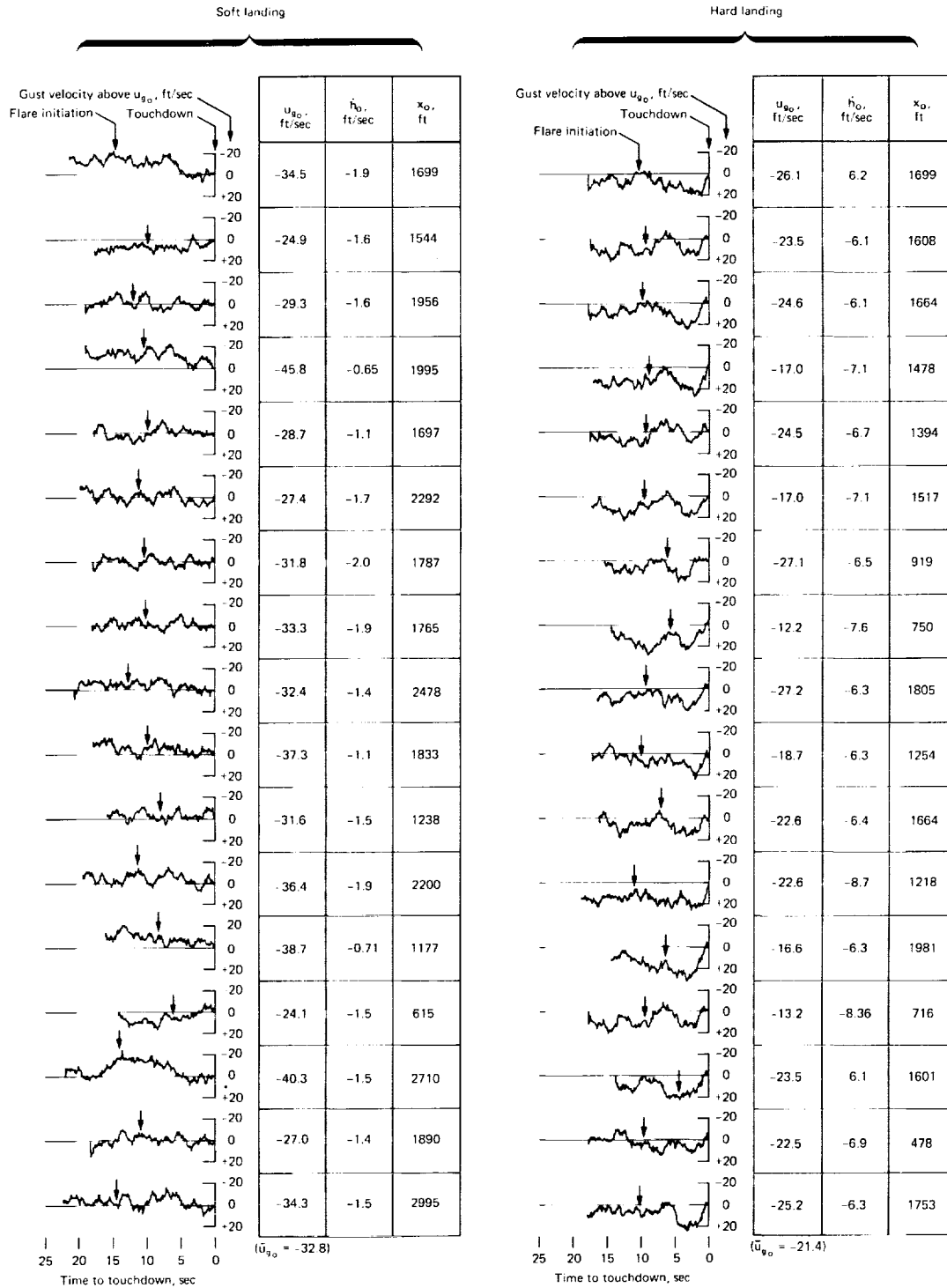


Figure 20.— Horizontal gust patterns that caused hard and soft landings;  $\bar{u}_{gx} = 30$  ft/sec,  $\sigma = 6$  ft/sec.

terminal sink rates and 17 flights with low terminal sink rates selected randomly from the 700 flight samples. It was pointed out earlier in the section pertaining to flights under steady wind conditions that the absolute magnitude of the wind is of little importance in the landing performance. For that reason, the horizontal reference line, in each graph, was drawn to intersect the ordinate at the wind velocity at touchdown. A vertical arrow indicates the time of the flare step command in pitch. In most hard landings first an increase and then a reduction of head wind occurs, meaning a sudden loss of lift. This also is indicated by the average wind velocity at touchdown of the 17 hard landings, which is 8.5 feet below the average wind velocity of 30 ft/sec. In contrast, the average wind at touchdown is close to the average wind velocity for the soft landings. Also, at touchdown, the wind velocity varies less and the large low frequency components are not present.

### Touchdown Performance of the Landing System

The method of calculating the overall probability distribution of sink rate at touchdown is described in reference 13. Besides needing the probability distribution of  $\dot{h}_0$  at a given turbulence level, one also needs the probability distribution of the turbulence magnitude, provided there is turbulence. The only probability distribution of  $\sigma_{ug}^2$  available for landings was given in reference 13. A corrected version of this distribution, which had unit area as required for a probability distribution, was provided by Hawker, Siddeley Aviation, Ltd., through private communication (see fig. 21). This probability distribution was divided into eight intervals, and runs were made with  $\sigma_{ug}^2$  at the center of each interval. The probability distribution for  $\dot{h}_0$  for a given gust variance was weighted with the probability that this variance occurs, and the overall distribution of exceeding  $\dot{h}_0$  was calculated and is shown in figure 22 (curve 1) for the complete range for turbulent conditions shown in figure 21. For curve 2, landings in turbulence above  $\sigma_{ug} = 5$  ft/sec are excluded. The results for both curves are similar to those given in reference 13, which includes data of actual landings. The dashed portions of the curves are extrapolations of the available data to a probability of  $10^{-6}$ . This value is a commonly used design goal for automatic landing systems.

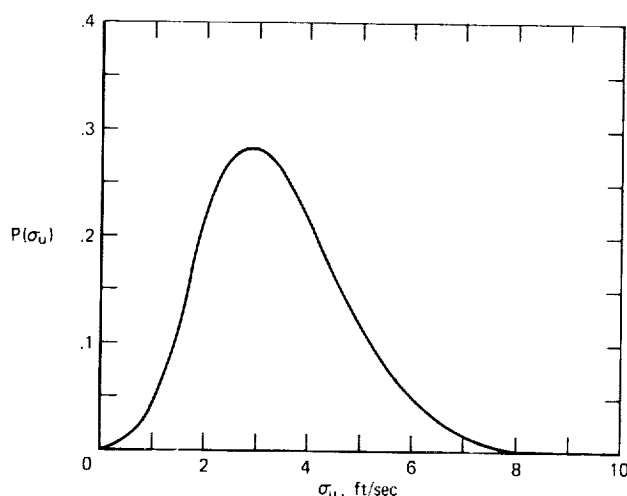


Figure 21.— Horizontal gust distribution; all weather conditions, wind limit 20 knots.

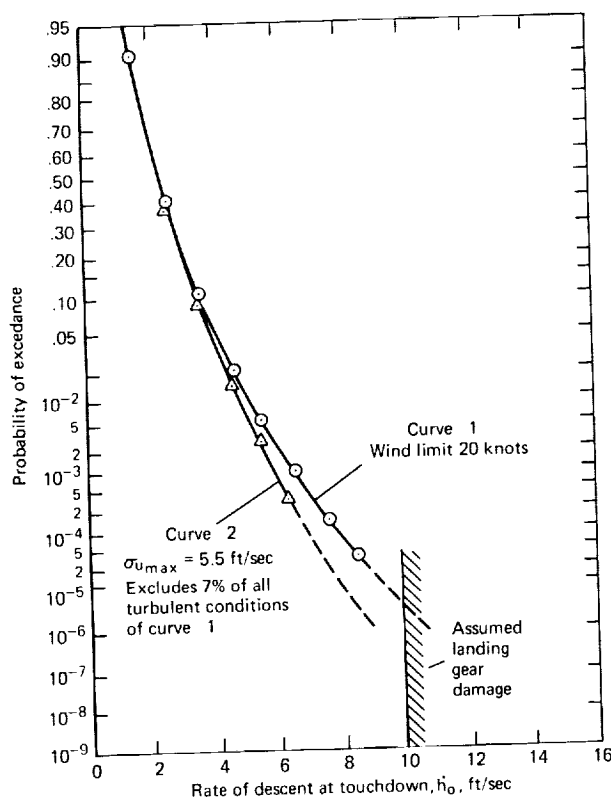


Figure 22.— Probability of exceeding a rate of descent (a straight line on this graph would indicate a normal distribution.)

Clearly, if the results actually reflect reality, automatic landings with the system studied should not be attempted in more than moderate turbulence for landing gear damage probability to be less than  $10^{-6}$ . This would mean that a certain percentage of all automatic landings should not be attempted because of turbulent conditions.

#### Performance of the System With Reduced Sampling Rates

It is of interest to know the minimum computation cycle rate, which does not compromise performance of the system. Table 5 shows the performance of the final version of the system for different sample time intervals. For the interpretation of these data one must remember that the aircraft equations of motion and of stability augmentation were still solved at the rate of 10 times per second, and only the control equations were solved less often. Also, the parameters for the control equations were recomputed and adjusted for the specific sample time being tested (e.g., the coefficients of the difference equations are a function of the sampling time).

Table 5(a) summarizes the glide-slope tracking performance changes with sampling time. The flare initiation conditions,  $x$  and  $h$  at 75 feet altitude (see footnote in table 5), are closer to the desired conditions for 0.1 and 0.2 second sampling intervals than for the larger intervals, as seen from the increase in variance for these quantities. Also, the flight-path tracking error standard deviation for tracking the glide slope,  $\sigma_{h_g}$ , increases with increasing sampling time.

Table 5(b) shows that for touchdown, as intervals become longer, there is a gradual decline in performance. The airplane tends to land harder and farther down the runway, and the touchdown pitch angle tends to be smaller. All three parameters have increased variations. A sink-rate frequency table is included to show the increase in hard touchdowns when  $T$  is increased.



TABLE 5.— PERFORMANCE DEGRADATION DUE TO INCREASE IN SAMPLE TIME INTERVAL  
[ $v_{xg} = -30$  ft/sec]

(a) Flight conditions before flare at  $h = 75$  ft

t	$\bar{h}^1$	$\sigma_{\bar{h}}$	$\bar{x}^1$	$\sigma_{\bar{x}}$	$\bar{h}_e$	$\sigma_{\bar{h}_e}$
0.1	-10.7	1.4	-1463	130	-0.98	12.3
.2	-10.4	1.9	-1462	140	-1.0	13.2
.4	-10.7	2.2	-1472	150	-1.4	14.1
.6	-10.5	2.2	-1483	140	-0.8	21.8
.8	-10.99	2.3	-1475	160	-2.1	17.7

<sup>1</sup> Ground track distance to ground intercept of glide slope and rate of descent at  $h = 75$  ft,  $x = 1432.4$  ft, and  $h_{\text{nominal}} = -10.4$  ft/sec.

(b) Touchdown

									No. of touchdowns within indicated sink rate limits (ft/sec)								
t	$\bar{h}_0$ no wind	$\bar{h}_0$	$\sigma_{\bar{h}}$	$x_0$ no wind	$\bar{x}_0$	$\sigma_{\bar{x}_0}$	$\bar{\theta}$	$\sigma_{\bar{\theta}}$	0-1	1-2	2-3	3-4	4-5	5-6	6-7	7-8	8-9
0.1	2.02	2.77	1.3	1560	937	580	0.0894	0.0088	5	27	35	15	10	6	2	0	0
.2	↓	2.78	1.2	↓	1034	620	.0879	.0084	6	26	27	26	10	3	2	0	0
.4	↓	2.90	1.3	↓	1073	630	.0876	.0088	3	20	38	21	10	3	4	1	0
.6	↓	3.13	1.4	↓	1101	660	.0865	.0091	4	21	23	27	14	7	2	2	0
.8	↓	3.73	1.9	↓	1344	710	.0617	.022	5	7	28	24	15	9	4	5	2

# Performance of the System With Randomly Missing Computation Cycles

Randomly missing a few percent of the control computation cycles had little effect on the landing performance. A random number generator at each sample interval was used in deciding whether or not to skip the control computations. An example with 5 percent missing samples is given in table 6. The effect is relatively small for the following two reasons: First, during the missed computation cycles, the control commands are simply frozen to the last commanded value, and are therefore not far from the correct value, and second, the system is a closed-loop feedback system in which errors built up during a missed cycle are corrected by subsequent increased control. Even in the extreme case for an average of 50 percent missing computation cycles the performance declines only slightly, as evidenced by the increased touchdown distance dispersion. However, the table for sink rate at touchdown shows that hard landings will occur if the sampling rate is reduced randomly. This indicates that for the flare, samples should not be skipped.

TABLE 6.— PERFORMANCE DEGRADATION DUE TO MISSING COMPUTATION CYCLES

[t = 0.1 sec, 20 ft/sec head wind]

(a) Flight conditions before flare at h = 75 ft

Percent missing samples	$\bar{h}$	$\sigma_{\bar{h}}$	$\bar{x}$	$\sigma_{\bar{x}}$	$\bar{h}_e$	$\sigma_{\bar{h}_e}$
0	10.7	1.4	1463	130	0.99	12.3
5	11.06	1.2	1462	110	-0.899	9.55
50	11.21	1.8	1462	130	-1.47	12.9

(b) Touchdown

Percent missing samples	$\bar{h}$	$\sigma_{\bar{h}}$	$\bar{x}$	$\sigma_{\bar{x}}$	No. of touchdowns within indicated sink rate limits (ft/sec)								
					0-1	1-2	2-3	3-4	4-5	5-6	6-7	7-8	8-9
0	2.77	1.3	937	580	5	27	35	15	10	6	2	0	0
5	2.49	1.0	1375	440	8	28	36	19	6	3	0	0	0
50	2.76	1.3	1228	880	4	27	38	18	4	6	1	1	1

## CONCLUSIONS

The study has been concerned with automatic pitch axis control for the approach and landing of a large jet transport aircraft by means of a general purpose digital computer. The study considered the effects of wind shears and turbulence and assumed error free ILS data and knowledge of altitude, vertical velocity, vertical acceleration, pitch attitude, and pitch rate.

The following conclusions were reached from this simulation study.

1. The chosen method of representing analog filters by difference equations was efficient and adequate. The frequency with which the control laws must be solved without loss of performance was relatively low, once every 0.2 second. (The required sampling rate for data acquisition and filtering may be appreciably higher.)

2. Several flare laws implemented in this investigation decreased the variability of the landing performance in the face of gust disturbances.

3. When the digital computer has other functions besides control (navigation, fuel management, measurement data smoothing and filtering, etc.), it is possible to skip randomly up to 50 percent of the computation cycles without affecting the flight-path control, except the flare, to any great extent.

4. Sink rate at touchdown is critically affected by transient wind shear starting during the flare. Therefore, an accurate gust gradient model of the turbulence near the ground is needed to predict the overall touchdown performance of automatic landing systems. Such a completely accurate gust model does not exist at this time.

5. The Monte Carlo method of the study of hard landings presents a computer time problem. Since records of turbulence that cause hard landings are distinctively different from those that do not, it would be possible by means of a computer program to identify those simulated or measured turbulence records that may cause hard landings. If the probability of occurrence of such severe turbulence samples were determined as well, much computer time would be saved.

Ames Research Center

National Aeronautics and Space Administration

Moffett Field, Calif., 94035, June 19, 1970

## APPENDIX A

### SIMULATION OF THE STABILIZED AIRPLANE

In modern analog autopilots, control commands generated by the various autopilot control modes are not applied directly to the actuators. Instead, the control modes provide commands to a stabilized aircraft. In the case of the pitch axis control, pitch commands and velocity commands are supplied to the stabilization loop which in turn generates elevator and throttle position commands. In conventionally designed systems, the important state variables are fed back in a sequence of minor and major loops. Each successive feedback serves a different major function and involves different types of measurement and accuracy problems. This is in contrast to optimum control approaches where all state variables are fed back to meet a global performance criterion (see ref. 14, appendix E, for an optimal control approach to the flare law design). The conventional approach has the advantage of simplicity and economy, since the airplane is already stabilized for all control modes. In this section, the aircraft, aircraft stabilization, and the resulting aircraft performance will be discussed. The system to be analyzed is shown in figure 1.

Both the airplane and the automatic landing system are simulated on the same digital computer. With the digital integration technique used, it was found that the airplane equations of motion had to be solved at least once each 0.1 second in aircraft time to result in a stable performance equivalent to an analog simulation. The Fortran IV simulation program was written so that the equations for analog system components were solved at the same rate as the aircraft equations of motion. The automatic control laws could be solved more slowly at any submultiple rate of the aircraft equations of motion. The solution rate of the aircraft equations of motion was adjusted so that any slow solution rate for the control equations could be simulated. The program was written either to run in real time or as fast as the computer could solve the equations. Fast runs at a computer cycle rate of 0.01 second per each 0.1 second aircraft time for both aircraft equations of motion and control equations allowed a 4-minute landing operation to be simulated in 24 seconds.

### AIRPLANE EQUATIONS

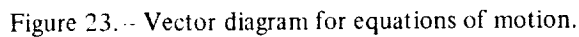
#### Equations of Motion

The equations of motion of a jet transport in its landing configuration are represented in figure 1 by the block labelled aerodynamics, which shows the input and output variables. The stability derivatives and other characteristics are given in table 7. The airplane was considered to be representative of the current class of turbojet transport. Also, performance data were available from the analog simulation described in reference 2, which allowed comparison with the digital simulation for program verification.

The equations of motion are simplified versions of those given in reference 2 modified to include the effect of wind. The modifications, which include removal of the lateral degrees of freedom and the effects of the landing gear contacting the ground, are straightforward and will not be discussed in detail.

TABLE 7.— AIRCRAFT PARAMETERS

Lift	
$C_L(\alpha)$	$0.19 + 5.3 \alpha$
$(\Delta C_L)_{\delta_f}$	$0.23 + 0.55 \delta_f$
$C_{L\delta_e}$	0.302
$C_{Lq}$	7.68
$(\Delta C_L)_{GE}$	$0.063(C_{L_\infty})\epsilon_{GE}$
Drag	
$C_D(\alpha)$	$0.03 + 0.08824 \alpha + 1.8182 \alpha^2$
$(\Delta C_D)_{\delta_f}$	$(0.126 + 0.473 \alpha) \delta_f$
$(\Delta C_D)_{GE}$	$(-0.02 - 0.332 \alpha) \epsilon_{GE}$
Pitch	
$C_{m_0}$	0.09
$C_{m_\alpha}$	-1.062
$C_{m\delta_e}$	-0.923
$C_{m\delta_f}$	-0.103
$C_{m\dot{\alpha}}$	-4.01
$C_{mq}$	-12.3
$(\Delta C_m)_{GE}$	$-0.066(C_{L_\infty})\epsilon_{GE}$
$(\Delta C_m)_{LG}$	-0.01
Ground effect factor	
$\epsilon_{GE}$	$0.972e^{-h/17}$
$h$	wheel weight
Air density	
$\rho$	$2.377 \times 10^{-3} \text{ slug/ft}^2$
Geometric parameters	
Area, $S$	2758 ft <sup>2</sup>
Chord, $\bar{c}$	22.16 ft
Thrust offset, $d$	4.0 ft
Thrust angle, $i_T$	3.15°
Weight parameters	
Weight, $w$	200,000 lb
Inertia, $I_{yy}$	$3.9 \times 10^6 \text{ slug-ft}^2$



Therefore, there is a contribution from the

The aircraft rate equations were numerically integrated using the fourth-order Adams-Bashford algorithm. With this algorithm a solution rate of  $t = 0.1$  second was adequate for the basic aircraft equations of motion. For faster solution rates no significant differences in aircraft response were detected, while at slower rates the numerical solution became unstable.

1. The airframe is assumed to be a rigid body with all motion restrained to the vertical plane.
2. Earth is assumed to be flat, nonrotating, and fixed in inertial space.
3. The mass of the airplane is assumed to be constant during each flight.
4. The  $x$ - $z$  plane is a plane of symmetry in the aircraft.
5. Small angle approximations apply.

6. The air flow is assumed to be quasi-steady.

7. Initial flight conditions are for steady-state flight. Thus the problem can be started instantly in trimmed flight if the aircraft state variables are specified and the integration subroutines are initiated automatically.

As shown in figure 23, four orthogonal axes systems are used in the same vertical plane:

- $x_E, z_E$  earth-fixed axis system; z points along the gravity vector; origin at the intersection of the glide slope and ground
- $x_T, z_T$  trajectory axis system; reference frame with origin at aircraft center of mass, and the x-direction aligned with the tangent to the flight path
- $x, z$  wind axis system; aerodynamic frame of reference with the origin at the aircraft center of mass and the x-direction aligned with the relative wind vector
- $x_B, z_B$  body axis system; x-axis fixed to the aircraft principal axis along the centerline of the fuselage; origin at the aircraft center of mass

Figure 23 also identifies all other vector quantities and angles, which will appear in the following set of definitions and equations.

Wind components in the earth axis system (average wind + gust input) calculated in a turbulence subroutine:

$$\left. \begin{aligned} v_{x_g} &= \bar{v}_{x_g} + n_x \\ v_{z_g} &= \bar{v}_{z_g} + n_z \end{aligned} \right\} \quad (A1)$$

Wind components along and perpendicular to the inertial velocity vector:

$$\left. \begin{aligned} u_g &= v_{x_g} \cos \gamma - v_{z_g} \sin \gamma \approx v_{x_g} - v_{z_g} \gamma \\ w_g &= v_{x_g} \sin \gamma + v_{z_g} \cos \gamma \approx v_{x_g} \gamma + v_{z_g} \end{aligned} \right\} \quad (A2)$$

Magnitude of the air velocity relative to the center of mass of the airplane:

$$|V| = \sqrt{(v_E - u_g)^2 + w_g^2} \quad (A3)$$

Angle between relative wind and inertial velocity vector:

$$\alpha_g = \sin^{-1} \frac{w_g}{|V|} \quad (A4)$$

Aerodynamic angle of attack:

$$\alpha = \eta - \alpha_g \quad (A5)$$

Aerodynamic equivalent pitch rate due to gusts (ref. 16, p. 322):

$$q_g = \frac{\partial w_g}{\partial x} \approx \frac{w_{gw} - w_{gT}}{80} \quad (A6)$$

where 80 feet is the distance from wing to tail

Aerodynamic pitch rate:

$$q_a = q + q_g \quad (A7)$$

Aerodynamic angle-of-attack rate:

$$\dot{\alpha} = q - \gamma - q_g \quad (A8)$$

Pitch acceleration (inertial):

$$\begin{aligned} \dot{q} = & \frac{\rho S \bar{c} V^2}{2 I_{YY}} \left[ C_{m_0} + C_{m_\alpha} \alpha + C_{m_{\delta e}} \delta e + (\Delta C_m)_{\delta f} \right] \\ & + \frac{\rho S \bar{c}}{4 I_{YY}} V \left[ C_{m_q} q_a + C_{m_{\dot{\alpha}}} \dot{\alpha} \right] + \frac{dT}{I_{YY}} \end{aligned} \quad (A9)$$

Lift-to-mass ratio and drag-to-mass ratio in the wind axis system:

$$\left. \begin{aligned} \frac{L}{m} &= \frac{\rho S}{2m} V^2 \left[ C_L(\alpha) + C_{L_{\delta e}} \delta e + (\Delta C_L)_{\delta f} + (\Delta C_L)_{GE} \right] + \frac{\rho S \bar{c}}{4m} V C_{L_q} q_a \\ \frac{D}{m} &= \frac{\rho S}{2m} V^2 \left[ C_D(\alpha) + (\Delta C_D)_{\delta f} + (\Delta C_D)_{GE} \right] \end{aligned} \right\} \quad (A10)$$

Aerodynamic force-to-mass ratios transformed through  $\alpha_g$  to the trajectory axis system:

$$\left. \begin{aligned} \frac{F_z}{m} &= \left( \frac{L}{m} \right) \cos \alpha_g - \left( \frac{D}{m} \right) \sin \alpha_g \approx \frac{L}{m} - \left( \frac{D}{m} \right) \alpha_g \\ \frac{F_x}{m} &= \left( \frac{D}{m} \right) \sin \alpha_g + \left( \frac{L}{m} \right) \cos \alpha_g \approx \frac{D}{m} + \left( \frac{L}{m} \right) \alpha_g \end{aligned} \right\} \quad (A11)$$



Acceleration components in the trajectory axis system:

$$\dot{V}_E = \frac{T}{m} \cos \gamma - g \sin \gamma - \frac{F_x}{m} \approx \frac{T}{m} - g\gamma - \frac{F_x}{m} \quad (A12)$$

$$a_{z_T} = g \cos \gamma - \frac{T}{m} \sin (\eta + i_T) - \frac{F_z}{m} = g - \frac{T}{m} (\eta + i_T) - \frac{F_z}{m}$$

Derivative of the flight-path angle:

$$\dot{\gamma} = - \frac{a_{z_T}}{V_E} \quad (A13)$$

Integration of the inertial rates (fourth-order Adams-Bashford (see appendix B)):

$$\gamma = \int \dot{\gamma} dt ; \quad V_E = \int \dot{V}_E dt ; \quad q = \int \dot{q} dt ; \quad \theta = \int q dt \quad (A14)$$

Angle between the body axis and the flight-path vector:

$$\eta = \theta - \gamma \quad (A15)$$

Rate and position in the earth-fixed reference frame:

$$\left. \begin{aligned} \dot{h} &= V_E \gamma \\ h &= \int \dot{h} dt \\ x &= \int V \cos \gamma dt \approx \int V dt \end{aligned} \right\} \quad (A16)$$

This completes a computation cycle. The computation continues with the control equations and returns to equation (A1).

### Engine and Engine Servos

Although the simulated reference jet transport represents a four-engine airplane, in the longitudinal simulation only, one equivalent engine needs to be simulated. The engine performance from throttle adjustment to change in thrust is represented as a first-order lag with a time constant of 1.25 sec. The engine servo is also assumed to be linear and it is represented as a second-order system with a natural frequency of 10 rad/sec, a damping ratio of 0.7, and a steady-state gain of 1.0. This overall system from thrust command to response is represented as one difference equation in this simulation (see eq. (7) table 8). Advantages of this method are discussed in appendix B.

### Elevator, Elevator Servo, and Flaps

The elevator and elevator servo combination is described by equation (7) table 8 also. In this case the elevator time constant is 0.2 second, natural frequency is 10 rad/sec, the damping ratio is 0.7, and the steady-state gain is 0.8.

The flaps are represented as a strictly rate limited system. Upon a change in flap command, they advance at a rate of 0.035 rad/sec until the new command value is reached.

## AUTOMATIC FLIGHT-PATH STABILIZATION

To control the flight path of an airplane automatically, it would be desirable to control the flight-path angle  $\gamma$  directly. However, there is no output control variable that directly controls  $\gamma$ . Also, for the basic airplane, for small deviations from horizontal flight, the steady-state flight-path angle is proportional to thrust for a constant pitch attitude, and the steady-state velocity decreases linearly with increase in pitch for constant thrust. Moreover, for short-period response, pitch does control the flight-path angle and pitch and pitch rate can be measured with gyros. To make short and long term responses agree, the aircraft is stabilized in the following manner. The airspeed of the aircraft is kept nearly constant by means of an autothrottle, and a pitch control loop maintains the flight path.

### Pitch Control Loop

The pitch axis of the aircraft is controlled through an inner feedback loop to follow the pitch commands from the autopilot (fig. 1). The command signal is differenced with a pitch attitude signal for position feedback, and a filtered pitch rate signal for damping. The pitch rate filter, called a washout filter, responds quickly to a change in pitch rate, and does not respond to constant rates. The filter has been included for realism, since it would have been needed for banked turns which represent a constant pitch rate. The filter step response is  $k \exp(-t/\tau)$ , where  $k = 0.5$  and  $\tau = 4$  sec. Since there is no integration in the forward path of the pitch control loop, the error signal at the summing junction is not driven to zero for a given pitch command. Hence, for steady state,  $\theta = k\theta_c$  where  $k$  is less than unity. This is alright in the automatic system, since the inner loop forms part of the forward path of the outer loop. The outer loop does contain integration to null flight-path errors. In the simulation, the pitch control loop equations are solved at the same rate as the airplane equations of motion, since in an actual system this loop might remain an analog loop. The response of the airplane will be discussed following the description of the autothrottle.

### Autothrottle

The autothrottle maintains constant airspeed by generating a thrust command signal to drive the throttle servo (fig. 24). The command signal is derived from three sources, the airspeed error, the longitudinal acceleration, and the pitch command. These three signals are further processed as follows. To provide an augmented airspeed error signal, the measured airspeed is summed with the airspeed reference and then summed with the output of a fore-aft accelerometer. The signal is then filtered in a blender filter (ref. 4). In effect, in turbulence the measured airspeed is heavily filtered so that the thrust command does not respond to gust inputs, whereas without turbulence the airspeed is not filtered.

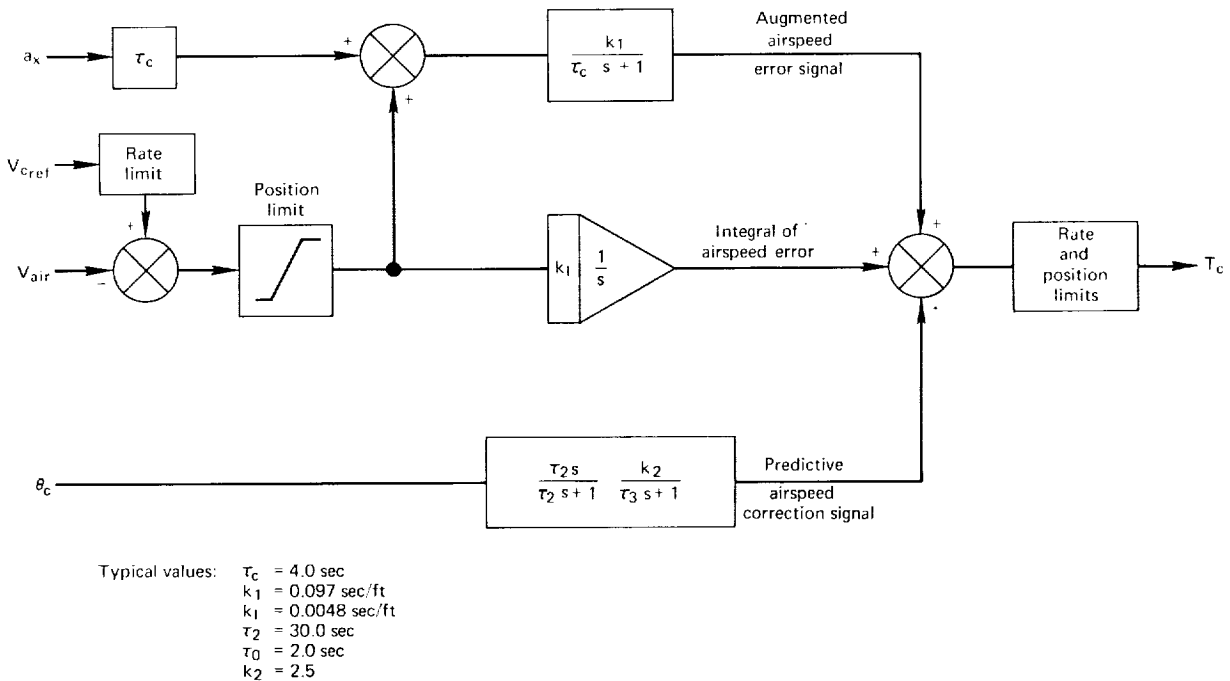


Figure 24.— Autothrottle.

The response of the system described so far is not fast enough to maintain a constant airspeed during pitch maneuvers such as those encountered while tracking an ILS glide-slope beam. To compensate for this slow response, a predictive thrust command is derived from processing pitch command changes through a wash-out filter in sequence with a low pass filter. The augmented airspeed error signal, integral of airspeed error signal, and predictive thrust command are summed to form the thrust command signal. To prevent heavy throttle activity in turbulent conditions a rate limiter is required plus a position limit to prevent the thrust from being set dangerously low.

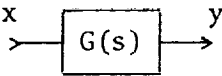
In the simulation a steady-state thrust command will result in an equal engine thrust. In an actual autothrottle system only changes in throttle settings are commanded. Thrust magnitude is not commanded since actual thrust is not directly measured. However, the simulation is adequate, because changes in thrust settings are commanded only from the velocity errors and not from thrust errors.

## APPENDIX B

### SIMULATION OF LINEAR SYSTEMS WITH DIFFERENCE EQUATIONS

The traditional method of simulating linear systems by analog computer is to solve the differential equations of the system in terms of the highest derivative and integrate. However, in digital simulation, when the integration is carried out numerically, it can be a lengthy process that may be unstable for large sampling intervals. Simulating a linear system with the chosen difference equation is more efficient than using numerical integration techniques and is numerically stable independent of the sampling interval (ref. 17).

The difference equation for one of the linear filters used in this simulation will be derived to provide a concrete example of the procedure. The transfer function of the wash-out filter used in the pitch stabilization loop is

$$G(s) = \frac{y(s)}{x(s)} = \frac{ks}{s + a}$$


The first step is to find the time response of the filter to a unit step input.

$$y(s) = \frac{ks}{s + a} \frac{1}{s} = \frac{k}{s + a}$$

$$y(t) = ke^{-at}$$

Next, find the  $z$  transform of  $y(t)$ .

$$y(z) = \frac{kz}{z - e^{-aT}}$$

Factor the  $z$  transform of a unit step function out of the expression for  $y(z)$ .

$$z(\text{unit step}) = \frac{z}{z - 1}$$

$$y(z) = k \frac{z - 1}{z - e^{-aT}} \frac{z}{z - 1}$$

Since the response to a general input is wanted, replace the step input by a general input  $x(z)$ . The actual input is approximated by a stair-step function that can be described by a linear combination of unit step functions and is equal to the general input at the sampling points.

$$y(z) = k \frac{z - 1}{z - e^{-aT}} x(z)$$

If we cross multiply,

$$(z - e^{-aT})y(z) = k(z - 1)x(z)$$

divide by  $z$ ,

$$\left(1 - \frac{e^{-aT}}{z}\right)y(z) = k\left(1 - \frac{1}{z}\right)x(z)$$

transform to the discrete time domain, remembering that  $(1/z)y_n = y_{n-1}$

$$y_n - e^{-aT}y_{n-1} = k(x_n - x_{n-1})$$

and rearranging, the final form of the difference equation is obtained:

$$y_n = e^{-aT}y_{n-1} + k(x_n - x_{n-1})$$

At the sampling points, the difference equation is the exact solution for the response of the equivalent analog system to a stair-step function input. Therefore, the solution does not become numerically unstable for large sampling intervals. However, the output of the system will be realistic only if the sampling is done frequently enough to result in a stair-step waveform which is a good approximation of the original continuous input waveform.

For comparison, the equations for the above filter using numerical integration (fourth-order Adams-Bashford) are:

$$y_n = y_{n-1} + \frac{T}{24} (55\dot{y}_n - 59\dot{y}_{n-1} + 37\dot{y}_{n-2} - 9\dot{y}_{n-3})$$

$$\dot{y}_n = -ay_n + kx_n$$

The computation efficiency of the difference equation is obviously better than that of the numerical integration technique. Also, this numerical integration method becomes numerically unstable for large sampling intervals, as confirmed during the investigation.

Difference equations were used to simulate the aircraft control and automatic stabilization systems, to replace the analog autopilot with a digital version, and to generate the turbulent wind components.

The aircraft control system simulator consists of a throttle servo with engine lag and an elevator servo with an elevator surface lag. Both of these servos have the same general form, a second-order transfer function with 0.7 critical damping in series with a first-order low pass filter. The form of the total transfer function and the corresponding difference equation are shown in section 7 of table 8.

The washout filter in the stability augmentation system discussed above is simulated by the difference equation of section 1 in table 8.

All of the linear control laws in the autopilot were mechanized by difference equations to simulate a digital autopilot. The various control transfer functions are listed in sections 8 through 10 in table 8.

The generation of the wind turbulence components requires the filtering of wide-band noise for spectrum shaping. Filters were simulated by the difference equations in sections 2 and 3 in table 8.

TABLE 8.— DIFFERENCE EQUATIONS USED IN THIS SIMULATION

[Plus others of interest in control simulations]

Eq.	Transfer function	Step response	Difference equation	Coefficient for difference equation (T = sampling interval)
1	$\frac{ks}{s+a}$	$ke^{-aT}$	$y_n = C_1 y_{n-1} + k(x_n - x_{n-1})$	$C_1 = e^{-aT}$
2	$\frac{k}{s+a}$	$\frac{k}{a} (1 - e^{-aT})$	$y_n = C_1 y_{n-1} + D x_{n-1}$	$C = e^{-aT}$ $D = \frac{k}{a} (1 - e^{-aT})$
3	$\frac{k(s+b)}{(s+a)^2}$	$k \frac{b}{a^2} + k \left( \frac{a-b}{a} t - \frac{b}{a^2} \right) e^{-aT}$	$y_n = C_1 y_{n-1} + C_2 y_{n-2} + D_1 x_{n-1} + D_2 x_{n-2}$	$C_1 = 2e^{-aT}$ $C_2 = -e^{-2aT}$ $D_1 = k \left[ \frac{b}{a^2} + e^{-aT} \left( \frac{a-b}{a} T - \frac{b}{a^2} \right) \right]$ $D_2 = k \left[ \frac{b}{a^2} (e^{-aT} - 1) - \frac{a-b}{a} T \right] e^{-aT}$
4	$\frac{ks(s+b)}{(s+a)^2}$	$k[(b-a)T + 1]e^{-aT}$	$y_n = C_1 y_{n-1} + C_2 y_{n-2} + kx_{n-1} + D_1 x_{n-2} + D_2 x_{n-3}$	$C_1 = 2e^{-aT}$ $C_2 = -e^{-2aT}$ $D_1 = k \left\{ [(b-a)T - 1]e^{-aT} - 1 \right\}$ $D_2 = -k - D_1$
5	$\frac{k}{(s+a)^2 + b^2}$ complex roots $s = -a \pm jb$	$\frac{k}{(a^2 + b^2)}$ $+ \frac{ke^{-aT}}{b(a^2 + b^2)^{1/2}} \sin(bT - \psi)$ $\psi = \tan^{-1} \frac{b}{-a}$	$y_n = C_1 y_{n-1} - C_2 y_{n-2} + D_1 x_n + D_2 x_{n-1} + D_3 x_{n-2}$	$k_1 = \frac{k}{\sqrt{a^2 + b^2}}, \quad \psi = \tan^{-1} \frac{b}{-a}$ $C_1 = 2e^{-aT} \cos bT$ $C_2 = e^{-2aT}$ $D_1 = k_1 \left( \frac{1}{\sqrt{a^2 + b^2}} - \frac{\sin \psi}{b} \right)$ $D_2 = k_1 \left[ \frac{-2e^{-aT} \cos bT}{\sqrt{a^2 + b^2}} + \sin \psi + e^{-aT} \sin(bT + \psi) \right]$ $D_3 = k_1 e^{-aT} \left[ \frac{e^{-aT}}{\sqrt{a^2 + b^2}} - \frac{\sin(bT + \psi)}{b} \right]$

TABLE 8.— DIFFERENCE EQUATIONS USED IN THIS SIMULATION — Continued  
[Plus others of interest in control simulations]

Eq.	Transfer function	Step response	Difference equation	Coefficient for difference equation (T = sampling interval)
6	$\frac{k}{(s+a)(s+b)}$ real roots	$\frac{k}{ab} + \frac{k(be^{-aT} - ae^{-bT})}{ab(a-b)}$	$y_n = C_1 y_{n-1} - C_2 y_{n-2} + D_1 x_{n-1} + D_2 x_{n-2}$	$C_1 = e^{-aT} + e^{-bT}$ $C_2 = e^{-(a+b)T}$ $D_1 = \frac{k}{ab} \left( \frac{be^{-aT} - ae^{-bT}}{a-b} + 1 \right)$ $D_2 = \frac{k}{ab} \frac{ae^{-aT}(e^{-bT} - 1) - be^{-bT}(e^{-aT} - 1)}{a-b}$
7	$\frac{k}{(s+c)[(s+a)^2 + b^2]}$ complex roots $s = -a \pm jb$ real root $s = -c$	$B_1 - B_2 e^{-cT} + B_3 e^{-aT} \sin(bT - \psi)$ where: $B_1 = \frac{k}{c(a^2 + b^2)}$ $B_2 = \frac{k}{c[(a-c)^2 + b^2]}$ $B_3 = \frac{k}{b[(a^2 + b^2)[(a-c)^2 + b^2]}^{1/2}$ $\psi = \tan^{-1} \frac{b}{-a} + \tan^{-1} \frac{b}{c-a}$	$y_n = C_1 y_{n-1} + C_2 y_{n-2} + C_3 y_{n-3} + D_1 x_n + D_2 x_{n-1} + D_3 x_{n-2} + D_4 x_{n-3}$	$\phi = \tan^{-1} \frac{b}{-a} + \tan^{-1} \frac{b}{c-a}$ $A_1 = \frac{k}{c(a^2 + b^2)}$ $A_2 = \frac{k}{c[(a-c)^2 + b^2]}$ $A_3 = \frac{k}{b[(c-a)^2 + b^2](a^2 + b^2)}$ $A_4 = e^{-aT} \sin(bT + \phi)$ $A_5 = 2e^{-aT} \cos bT$ $A_6 = e^{-2aT}$ $A_7 = e^{-cT}$ $A_{10} = -\sin \phi$ $C_1 = A_7 + A_5, \quad C_2 = -A_6 - A_5 A_7, \quad C_3 = A_7 A_6$ $D_1 = A_1 - A_2 + A_3 A_{10}$ $D_2 = -A_1(A_7 + A_5) + A_2(1 + A_5) + A_3(A_4 - A_{10} - A_{10} A_7)$ $D_3 = A_1(A_6 + A_5 A_7) - A_2(A_5 + A_6) + A_3(A_7 A_{10} - A_6 - A_6 A_7)$ $D_4 = -A_1 A_7 A_6 + A_2 A_6 + A_3 A_7 A_4$



TABLE 8.— DIFFERENCE EQUATIONS USED IN THIS SIMULATION — Concluded  
 [Plus others of interest in control simulations]

Eq.	Transfer function	Step response	Difference equation	Coefficient for difference equation (T = sampling interval)
8	$\frac{k[1 + (a/s)]}{\tau s + 1}$	$k[1 - a\tau + aT + (a\tau - 1)e^{-T/\tau}]$	$y_n = C_1 y_{n-1} - C_2 y_{n-2} + D_1 x_{n-1} - D_2 x_{n-2}$	$C_1 = 1 + e^{-T/\tau}$ $C_2 = e^{-T/\tau}$ $D_1 = k[aT + (1 - \tau a)(1 - C_2)]$ $D_2 = k[a\tau C_2 + (1 - \tau a)(1 - C_2)]$
9	$\frac{k}{s(\tau s + 1)}$	$a(T - \tau + \tau e^{-T/\tau})$	$y_n = C_1 y_{n-1} - C_2 y_{n-2} + D_1 x_{n-1} + D_2 x_{n-2}$	$C_1 = 1 + e^{-T/\tau}$ $C_2 = e^{-T/\tau}$ $D_1 = a[T + \tau(C_2 - 1)]$ $D_2 = a[\tau - C_2(T + \tau)]$
10	$k\left(1 + \frac{a}{s}\right)$	$k + kaT$	$y_n = y_{n-1} + kx_n + Cx_{n-1}$	$C = k(aT - 1)$
11	$\frac{ks}{(s + a)(s + b)}$	$\frac{k(e^{-aT} - e^{-bT})}{b - a}$	$y_n = C_1 y_{n-1} - C_2 y_{n-2} + D(x_{n-1} - x_{n-2})$	$C_1 = e^{-aT} + e^{-bT}$ $C_2 = e^{-(a+b)T}$ $D = k \frac{(e^{-aT} - e^{-bT})}{b - a}$

## APPENDIX C

### FILTER GAIN CONSTANT ADJUSTMENT FOR THE DIGITAL TURBULENCE SIMULATION

For the turbulence simulation the variance of the gust must be generated correctly. From the discussion of the difference equations in appendix B, the overall digital generation of the turbulence noise sequence can be compared to a continuous system with sample and hold circuits as shown in figure 25. The output of this circuit, expressed as a sequence of numbers, is statistically identical with the number sequence derived in the digital program. Therefore, the knowledge can be used to calculate the ratio of output to input variance for both difference equations (eqs. (19) and (24)). The input noise sequence to the filter can be thought of as a random wave (see fig. 26). Its power spectrum is (see ref. 9 and fig. 27).

$$\Phi_X(\omega) = \frac{\sigma_X^2 T}{\pi} \left[ \frac{\sin(\omega T/2)}{\omega T/2} \right]^2 \quad (C1)$$

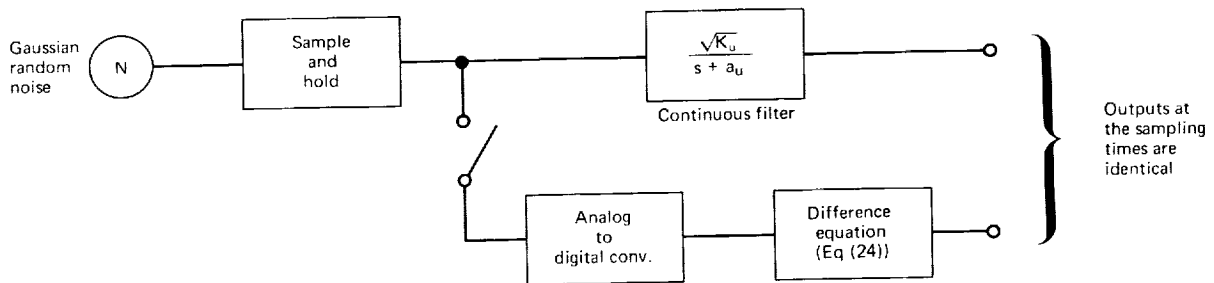


Figure 25.— Comparison of equivalent digital and analog turbulence generation.

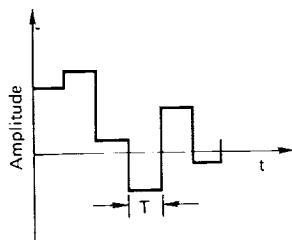


Figure 26.— Random wave.

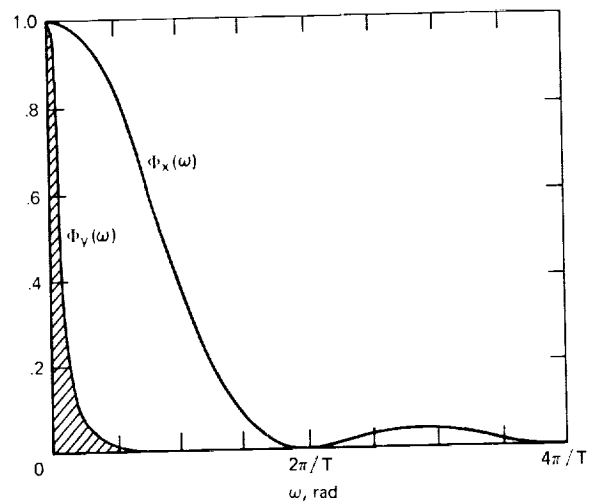


Figure 27.— Normalized power spectra,  $\Phi(0) = 1$ .

For example, it can be shown that at a sampling interval of  $t = 0.1$  sec the input spectrum is flat to 1 dB up to 2.5 Hz. This is sufficiently high, since a transport aircraft approximated as a rigid body does not respond to such high frequencies, and since the gust spectrum  $\Phi_Y(\omega)$  is a low frequency spectrum (see fig. 27). Higher frequencies will be attenuated as a result of the nonwhiteness of the input spectrum.

The ratio of output variance to input variance is calculated from

$$\sigma_{y_a}^2 = \int_0^{\infty} \Phi_X(\omega) |F(\omega)|^2 d\omega \quad (C2)$$

and

$$\sigma_{x_a}^2 = \int_0^{\infty} \Phi_X(\omega) d\omega \quad (C3)$$

From equation (16) of the text  $F(\omega)$  will be chosen so that

$$|F(\omega)|^2 = \Phi_Y(\omega) \quad (C4)$$

Using (C1) through (C4) gives the desired ratio

$$\begin{aligned} \frac{\sigma_{y_a}^2}{\sigma_{x_a}^2} &= \frac{\int_0^{\infty} (\sigma_X^2 T / \pi) \left\{ [\sin(\omega T / 2)] / (\omega T / 2) \right\}^2 \Phi_Y(\omega) d\omega}{\int_0^{\infty} (\sigma_X^2 T / \pi) \left\{ [\sin(\omega T / 2)] / (\omega T / 2) \right\}^2 d\omega} \\ &= \frac{(\sigma_X^2 T / \pi) \int_0^{\infty} \left\{ [\sin(\omega T / 2)] / (\omega T / 2) \right\}^2 \Phi_Y(\omega) d\omega}{\sigma_X^2} \end{aligned} \quad (C5)$$

with the approximation  $\{[\sin(\omega T / 2)] / (\omega T / 2)\}^2 = 1$  in the range where  $\Phi_Y(\omega)$  has significant energy

$$\frac{\sigma_{y_a}^2}{\sigma_{x_a}^2} = (T / \pi) \int_0^{\infty} \Phi_Y(\omega) d\omega = (T / \pi) \sigma_Y^2 \quad (C6)$$

An approach to exact equations for the output variance is to calculate it directly by expressing the difference equation involving input and output variables in terms of the input variable only.

$$y_n = \lim_{n \rightarrow \infty} \sum_{i=0}^n a_i x_i \quad (C7)$$

Since  $\sigma_{x_i}$  is the same for all  $x_i$ , and the  $x_i$  are independent, the variance of  $y_n$  will be

$$\sigma_y^2 = \sigma_X^2 \sum_{i=0}^{\infty} a_i^2 \quad (C8)$$

To find the  $a_i$  one writes the initial terms of the difference equation for the first few inputs and then deduces the functional relationship between  $a_i$  and  $a_{i+1}$ . The correctness of this solution is then checked by induction. Now the sum of the squares of these terms can be split into geometric series and derivatives of geometric series, which are all summable.

This method results in the following equation for  $\sigma_{u_a}^2$

$$\sigma_{u_a}^2 = \left[ \frac{2\sigma_u^2}{\pi a_u} \frac{(1 - e^{-a_u T})^2}{1 - e^{-2a_u T}} \right] \sigma_x^2 \quad (C9)$$

Similarly, the development for  $\sigma_w^2$  begins by defining  $C \triangleq e^{-awT}$  and rewriting (19), where  $D_1$  and  $D_2$  are defined as previously.

$$y_n = 2Cy_{n-1} - C^2y_{n-2} + D_1x_{n-1} + D_2x_{n-2} \quad (C10)$$

With this, after some algebra,

$$\sigma_w^2 = \left[ \left( D_1^2 + \frac{2D_1D_2}{C} + \frac{D_2^2}{C^2} \right) \frac{C(1+C^2)}{(1-C^2)^3} + \left( 2D_1^2 + 2\frac{D_1D_2}{C} \right) \frac{C^2}{(1-C^2)^2} + D_1^2 \frac{1}{1-C^2} \right] \sigma_x^2 \quad (C11)$$

For  $aT \ll 1$ , equations (C9) and (C11) reduce to (C6).

## REFERENCES

1. Johnson, Walter A.; and McRuer, Duane T.: Development of a Category II Approach System Model. Tech. Rep. 182-1, Systems Technology Inc., Dec. 1969.
2. Jackson, Charles T.; and Snyder, Thomas C.: Validation of a Research Simulator for Investigating Jet Transport Handling Qualities and Airworthiness Criteria During Takeoff. NASA TN D-3565, 1966.
3. Blakelock, John H.: Automatic Control of Aircraft and Missiles. John Wiley, N. Y., 1965.
4. Osder, S. S.: Avionics Requirements for All Weather Landing of Advanced SST's. Vol. I, Analysis of System Concepts and Operational Problems. Final Report, Sperry Phoenix. NASA CR-73092, 1967.
5. Hughes, N. H.; and Lazeby, G. P.: A Flight Experiment to Determine the Effects of Flare Entry Conditions on Automatic Landing Performance. Tech. Rep. 65283, Royal Aircraft Establishment, Dec. 1965.
6. Houbolt, John C.; Steiner, Roy; and Pratt, Kermit G.: Dynamic Response of Airplanes in Atmospheric Turbulence Including Flight Data on Input and Response. NASA TR R-199, 1964.
7. Batchelor, George K.: The Theory of Homogeneous Turbulence. Cambridge Univ. Press, 1953.
8. Pritchard, Francis E.: Turbulence and Terrain Environments Affecting Low-Altitude High-Speed Flight. Rep. CAL-FDM-393, Cornell Aeronautical Lab., July 1966. Presented at the IEEE/AIAA National Aerospace Electronics Conference, Dayton, Ohio, May 16-18, 1966.
9. Papoulis, Athanasios: The Fourier Integral and Its Applications. McGraw-Hill, N. Y., 1962.
10. Jones, J. G.: Gradient Properties of a Model of Stationary Random Turbulence. C. P. 998, Aeronautical Research Council, Great Britain, June 1968.
11. ,Anon.: Criteria for Approval of Category II Landing Weather Minima. FAA Advisory Circular AC 120-20, June 6, 1966.
12. Li, Jerome C. R.: Introduction to Statistical Interference. Edwards Bros., Inc., Ann Arbor, Michigan, 1959.
13. Hall, J. C.: The Effect of Low Altitude Gusts on Automatic Landing. AGARD Stability and Control, Pt. 2, Sept. 1966, pp. 831-853.
14. Merriam, C. W.: Optimization Theory and the Design of Feedback Control Systems. McGraw-Hill, N. Y., 1964.

15. Connelly, Mark E.: Simulation of Aircraft. NAVTRADEVCEP Rep. 7591-R-1, Servomechanisms Lab., MIT, Feb. 1958.
16. Etkin, Bernard: Dynamics of Flight Stability and Control. John Wiley, N. Y., 1959.
17. Anon.: Numerical Techniques for Real-Time Digital Flight Simulation. Publication E20-8186, International Business Machines, 1965.
18. Truxal, John G.: Automatic Feedback Control Systems Synthesis. McGraw-Hill, N. Y., 1955.



